EMBO
reports

The Tau/A152T mutation, a risk factor for frontotemporal-spectrum disorders, leads to NR2B receptor-mediated excitotoxicity

Jochen Martin Decker[1,†], Lars Krüger[1,†], Astrid Sydow[1,2], Frank JA Dennissen[1], Zuzana Siskova[1], Eckhard Mandelkow[1,2,3] & Eva-Maria Mandelkow[1,2,3,*]

Abstract

We report on a novel transgenic mouse model expressing human full-length Tau with the Tau mutation A152T (hTau[AT]), a risk factor for FTD-spectrum disorders including PSP and CBD. Brain neurons reveal pathological Tau conformation, hyperphosphorylation, mis-sorting, aggregation, neuronal degeneration, and progressive loss, most prominently in area CA3 of the hippocampus. The mossy fiber pathway shows enhanced basal synaptic transmission without changes in short- or long-term plasticity. In organotypic hippocampal slices, extracellular glutamate increases early above control levels, followed by a rise in neurotoxicity. These changes are normalized by inhibiting neurotransmitter release or by blocking voltage-gated sodium channels. CA3 neurons show elevated intracellular calcium during rest and after activity induction which is sensitive to NR2B antagonizing drugs, demonstrating a pivotal role of extrasynaptic NMDA receptors. Slices show pronounced epileptiform activity and axonal sprouting of mossy fibers. Excitotoxic neuronal death is ameliorated by ceftriaxone, which stimulates astrocytic glutamate uptake via the transporter EAAT2/GLT1. In summary, hTau[AT] causes excitotoxicity mediated by NR2B-containing NMDA receptors due to enhanced extracellular glutamate.

See also: **S Maeda** *et al*

Introduction

Familial tauopathies including FTDP-17 are often caused by mutations in the Tau gene (MAPT), which particularly occur in Tau's microtubule-binding repeat region [1]. MAPT mutations can lead to a partial loss of function due to a reduction in Tau's microtubule-binding capability or to a gain of toxic function by increasing the tendency of Tau to aggregate into filaments [2,3]. By contrast, the rare Tau p.A152T substitution is located outside the microtubule-binding domain in the N-terminal half of Tau. It has emerged as a risk factor for both frontotemporal dementias (FTDs) and Alzheimer's disease (AD), including progressive supranuclear palsy (PSP) and corticobasal degeneration (CBD) [4–7]. The mutation decreases Tau's binding to microtubules and increases the formation of Tau oligomers *in vitro* [7]. However, the consequences for neuronal function and the exact course of pathogenesis still remain elusive. We therefore generated a transgenic mouse line expressing the Tau-A152T mutation and characterized its pathology.

In healthy conditions, Tau is localized mainly in axons, stabilizes microtubules, and supports axonal transport processes [8,9]. Phosphorylation and detachment of Tau from microtubules following subsequent mis-sorting into cell bodies and dendrites may provoke axonal transport alterations [10,11], which in turn may disturb physiological conditions at postsynapses [12,13]. Presynaptic physiological disturbances in Tau models have been reported as well [14,15]. Phosphorylated Tau within dendritic spines has been proposed to impair synaptic transmission by decreasing the densities of postsynaptic α-amino-3-hydroxy-5-methyl-4-isoxazolepropionic acid (AMPA) and N-methyl-D-aspartate (NMDA) receptors [12] and causes calcium dysregulation [16]. Furthermore, dendritic Tau is thought to mediate Aβ-induced excitotoxicity and memory deficits in APP transgenic mice [13,17]. Tau plays a role in neuronal excitability and is required for Aβ and other excitotoxins to execute their degenerative effect, such as aberrant network activity and cognitive decline [13,18]. In primary neurons prepared from mice expressing mutant human APP tau allows Aβ oligomers to inhibit

1 German Center for Neurodegenerative Diseases (DZNE), Bonn, Germany
2 Max-Planck-Institute for Metabolism Research (Cologne), Hamburg Outstation, Hamburg, Germany
3 Caesar Research Center, Bonn, Germany
*Corresponding author. Tel: +49 2284 3302630; E-mail: eva.mandelkow@dzne.de
†These authors contributed equally to this work

axonal transport through activation of GSK3β [19]. Genetic ablation of Tau decreases spontaneous seizures in APP transgenic mice and even in a non-AD epilepsy model [20,21].

Tauopathies are characterized by pathological aggregation of Tau and massive cell loss in particular brain regions. In the case of PSP, this occurs in the basal ganglia and brain stem [22] but also in the hippocampus, which may be one factor contributing to cognitive decline. The molecular mechanisms of Tau-mediated neurotoxicity are not well understood and may be diverse. One suggested mechanism in AD is glutamate-mediated excitotoxicity which may lead to the stimulation of extrasynaptic NMDARs (containing NR2B-subunits) and promote Tau-dependent cell death [23]. Recently, impairments in glutamate metabolism were also reported in the hippocampus of transgenic mice overexpressing Tau-P301L [24,25].

When characterizing the new Tau A152T substitution (hTau[AT]) mouse model by biochemistry and immunohistochemistry, we noticed that the most prominent Tau pathology occurred in the mossy fiber pathway of the CA3 region. We therefore analyzed this region in acute and organotypic slices for structural and functional abnormalities. This revealed a distinct, excitotoxic phenotype which caused an increase in extracellular glutamate, a rise in intracellular calcium, combined with epileptiform activity and mossy fiber sprouting in the hippocampus. This was reminiscent of the situation in PSP patients, where increased seizure susceptibility was reported [26]. The effects were consistent with an overactivation of extrasynaptic NMDA receptors and could be prevented by pharmacological treatments stimulating the uptake of glutamate by astrocytic glutamate transporters (EAAT2/GLT1). These results agree well with observations from another mouse model based on the same mutation [27], which shows age-dependent neuronal loss, cognitive impairments, and spontaneous nonconvulsive epileptiform activity.

Results

Generation and phenotypic characterization of hTau[AT] mice

We generated a novel transgenic mouse model (hTau[AT]) expressing human full-length Tau (hTau40, 2N4R) with the PSP-related point mutation p.A152T (Fig 1A). The transgene is located in the ROSA26 locus [28] and its expression is controlled by the neuron-specific Thy1.2 promoter. This results in moderate overexpression levels in the hippocampus of heterozygous (+/−) and homozygous (+/+) hTau[AT] mice at an age of 14 months (Fig 1B). The molecular ratios of mutant hTau[AT] to endogenous mouse Tau protein in the hippocampus are ~1:1 (heterozygous) and 1.8:1 (homozygous mice) (Fig 1C). The hTau[AT] mRNA levels in transgenic heterozygous (1.00 ± 0.35 A.U.) and homozygous (2.19 ± 0.27 A.U.) mice (16 month) were in good agreement with the hTau/mTau protein expression ratios in hippocampi from transgenic animals (compare Fig 1C to D). Immunohistological analysis with the human Tau-specific antibody HT7 confirmed the higher hTau[AT] expression in the homozygous hTau[AT] mice (Fig 1E). Both types of mice show intense staining of the CA3-mossy fibers (Fig 1E, asterisks) and mis-sorting of the human Tau[AT] into the somato-dendritic compartment, a typical early feature of AD (Fig 1E, arrowheads). The hTau[AT]-expressing mice show hyperphosphorylated Tau (by antibodies pT217, AT180 (pSer235, pSer202), PHF1 (pSer396/pSer404), and AT8 (pSer202/pThr205); Fig 1F–I, respectively) and a pathological Tau conformation (antibody Alz-50, Fig 2A). Transgenic Tau is prominent in the axonal mossy fibers of the CA3 region (Fig 1E and H, asterisks) and is mis-sorted into the cell bodies of hippocampal pyramidal neurons (Fig 1E–I, arrowheads). Using two complementary techniques, Gallyas silver staining (Fig 2B) and sarcosyl extraction (Fig 2C), we could identify aggregated Tau species in 14-month-old mice. Interestingly, both hTau[AT] and mouse Tau was found in the sarcosyl-insoluble fraction indicating strong co-aggregation (Fig 2C). The ratio of mutant hTau[AT] to endogenous Tau within the sarcosyl-insoluble fraction is 0.7:1 (+/−) and 1.4:1 (+/+), demonstrating that endogenous mouse Tau is incorporated into Tau aggregates (Fig 2D).

Electron microscopy revealed typical ultrastructural hallmarks of hippocampal CA3 neuropil, including distinct mossy fiber boutons in the stratum lucidum that appeared intact, densely packed with clear synaptic vesicles in control animals (Fig 2E). By contrast, in transgenic age-matched animals, some presynaptic terminals were electron dense and filled with swollen synaptic

---

Figure 1. Expression of hTau[AT] causes Tau phosphorylation and mis-sorting in aged mouse hippocampi.

A   The diagram shows the domain structure of wild-type human Tau and the location of the substitution A152T (hTau[AT]). Tau domains are broadly divided into the N-terminal "projection domain" (amino acids M1-Y197) and the C-terminal "assembly domain" (amino acids S198-L441). The C-terminal assembly domain includes three or four pseudo-repeats (~31 residues each, R1–R4), which together with their proline-rich flanking regions (P1 and P2) constitute the microtubule-binding region. Repeat R2 (exon10) and the two near-N-terminal inserts (N1 and N2, exons 2 and 3) may be absent due to alternative splicing.

B   Blots showing expression of hTau[AT] (hTau, Mr ~67 kDa) and/or endogenous mouse Tau (mTau, Mr ~45–55 kDa) in the hippocampus of 10-month-old heterozygous (+/−) and homozygous (+/+) hTau[AT] mice in comparison to age-matched control (Ctrl) detected by pan-Tau antibody K9JA. Actin at 42 kDa serves as a loading control.

C   Quantification of (B). Ratio of hTau/mTau indicating a higher hTau[AT] expression in homozygous mice (~1.8) compared to heterozygous mice (~1.0). Each bar represents an average of n = 4 animals, error bars represent SEM.

D   Quantification of mRNA levels in hippocampi of heterozygous and homozygous hTau[AT] 16-month-old mice (n = 4 animals per group). Error bars indicate mean ± SEM.

E   Distribution of hTau[AT] visualized by the human Tau-specific antibody HT7 in the hippocampal CA3-region of hetero- and homozygous hTau[AT] mice at the age of 14 months. Notice the mis-sorted hTau[AT] in cell bodies and dendrites (arrowheads) of pyramidal neurons of the CA3 region and immunreactivity of the axons (mossy fibers, asterisks). By contrast, the control shows no immunoreactivity.

F   Elevated hTau[AT] expression causes Tau pathology inside area CA3 of the hippocampus. Note the increase in Tau phosphorylation probed with the antibody against pT217, a site upstream of the repeat domain. Arrowheads point to areas with phosphorylated and mislocalized Tau in cell somata of pyramidal neurons in area CA3.

G   Tauopathy detected by antibody AT180 specific for phosphorylation sites pT231 + pSer235 (arrowheads denote somato-dendritic mislocalized tau).

H   Antibody PHF-1 (phosphorylation sites pSer396 + pSer404) illustrates pathological phosphorylation of Tau due to hTau[AT] expression especially in stratum lucidum (asterisks) of area CA3 and pyramidal cell bodies (arrows).

I   Tau phosphorylation detected by antibody AT8 (pS202 + pT205) in stratum pyramidale of area CA3 (arrowhead). Note that immunoreactivity increases with expression level.

vesicles (Fig 2F, arrow). Interestingly, relatively high numbers of synapses, specifically with perforated postsynaptic densities, appeared intact in the stratum lucidum of transgenic animals with no obvious signs of degeneration (Fig 2F and J, asterisks). This finding is in apparent contrast to other animal models including a tau-aggregation model associated with the ΔK280 mutation and the classical murine models overexpressing APP/PS1 mutations [29,30]. Neuropathology in these models was generally associated with a profound and early reduction in the numbers of excitatory hippocampal synapses that was not apparent in our study even at

late disease stage (12–13 months). Signs of neuronal degeneration were obvious in pyramidal neurons; degenerating profiles were identified by a shrunken cell membrane plus a darkened cytoplasm, as well as darkened nucleoplasm and crenated nucleolemma within cell soma (Fig 2G, arrow). Furthermore, various degrees of structural abnormalities were detected in dendrites and axons (Fig 2G–J). Electron opaque, degenerating neuritic profiles were identified by an increase in mitochondrial density, presence of whorling membrane fragments, and numerous lysosome-like vacuoles (Fig 2J, arrow).
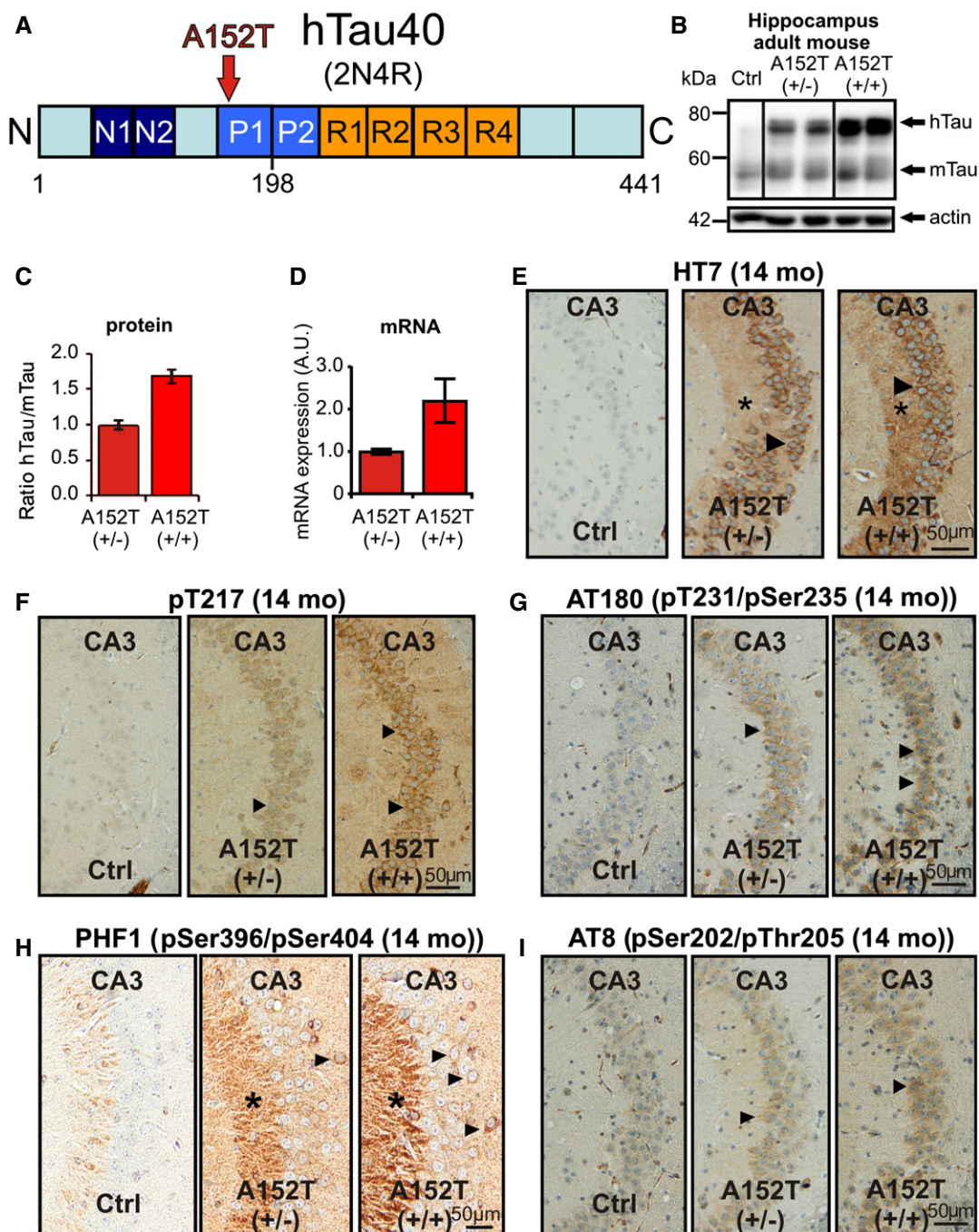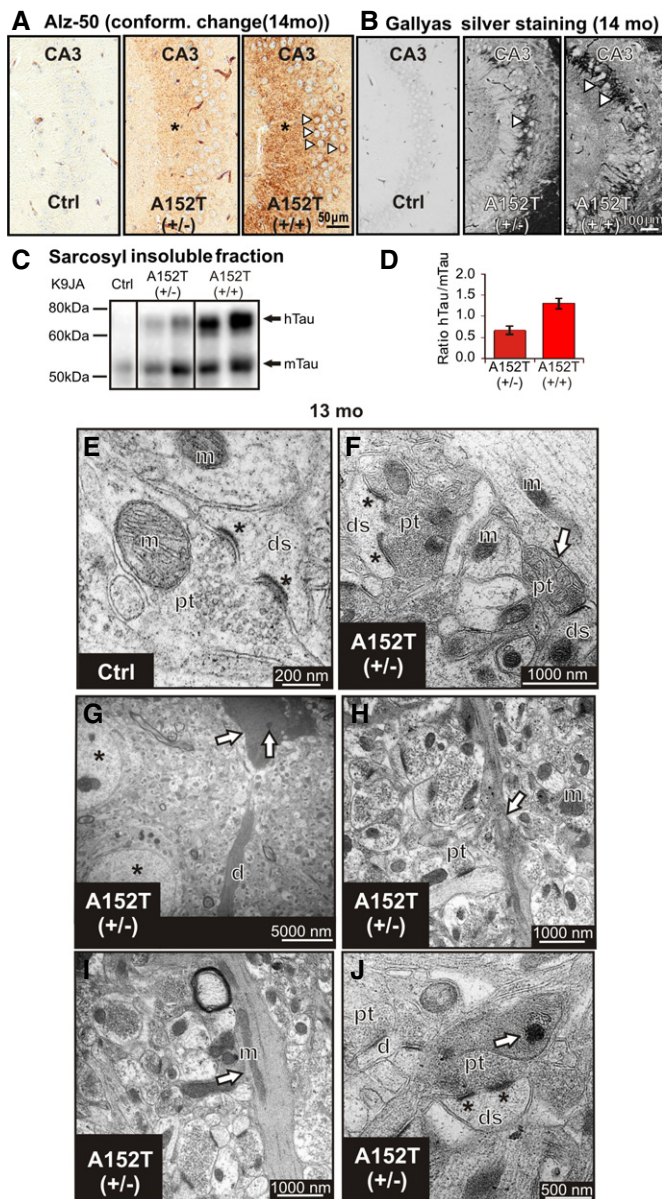

Figure 1.

A Alz-50 (conform. change(14mo))

B Gallyas silver staining (14 mo)

C Sarcosyl insoluble fraction

D

13 mo

Figure 2. Expression of hTau[AT] leads to pathological conformation and aggregation of Tau in the hippocampus of aged mice.

A Conformational change of Tau detected by ALZ-50 antibody immunoreactivity in stratum lucidum (asterisks) of area CA3 and somata in stratum pyramidale (arrowheads).

B Tau aggregation confirmed by Gallyas silver staining of NFTs bearing neurons in hetero- and homozygous hTau[AT] mice at 14 months of age compared to non-reactive control littermate mice. In homozygous hTau[AT] mice, the extent of neurofibrillary tangles (NFTs) visualized by Gallyas silver staining is enhanced compared to heterozygous hTau[AT] mice (white arrowheads). The control shows no silver-reactive Tau aggregates.

C Western blot analysis using the pan-Tau antibody K9JA indicates sarcosyl-insoluble Tau species of human hTau[AT] (upper band) and mouse Tau (mTau, lower band). Note the enhanced Tau aggregation in homozygous hTau[AT] mice compared to heterozygous hTau[AT] mice and control mice.

D Quantification of (C). The ratio of hTau[AT]/mTau indicates a stronger aggregation in the homozygous hTau[AT] mice (~1.4) compared to heterozygous hTau[AT] mice (~0.7) ($n = 4$ animals, error bars represent SEM).

E Electron micrograph of CA3 region of the hippocampus illustrating typical synapse with a perforated postsynaptic density (asterisks) in a control animal at 12 months. ds, dendritic spine; pt, presynaptic terminal; m, mitochondrium.

F Example of a degenerating synaptic bouton (arrow) containing swollen synaptic vesicles in proximity to a large terminal with a perforated postsynaptic density (asterisks) in a transgenic animal at 13 months.

G Electron-dense neuronal cytoplasm with dark nucleoplasm and various vacuoles (arrow) detected in CA3 pyramidal neurons (arrow) at 13 months in transgenic animals in proximity to normally appearing neurons (asterisks), degenerating apical dendrite (d).

H Neuropil of a transgenic animal (13 months) with a degenerating neuritic profile (arrow).

I Degenerating dendrite (arrow) in a transgenic animal with darkened cytoplasm and abnormally distributed mitochondria (arrow).

J Degenerating dendrite containing electron-dense whorling membrane fragments (arrow) in proximity to normally appearing synapses (synapse with a perforated postsynaptic density, asterisks).

of Tau with the pan-Tau antibody (Fig EV1A). In contrast, in hTau[AT] slices the human Tau appeared both in axons (Fig 3C asterisk) and dendrites (Fig 3C, right panel). Whereas the dendritic marker MAP2 was restricted to the dendritic shaft, Tau was also apparent in dendritic spines when hTau[AT] was expressed (Fig 3E, see also Fig EV1B, inset). The somato-dendritically mis-sorted Tau showed enhanced phosphorylation at the PHF1 epitope (pSer394/pSer404) already at DIV 10, but not in control littermate slices (Fig 3D).

Tau is hyperphosphorylated and mis-sorted due to hTau[AT] expression in hippocampal slice cultures

To further clarify whether hTau[AT] is mis-sorted into dendrites and dendritic spines, we used immunofluorescence in organotypic hippocampal slices. Organotypic hippocampal slices were derived from young heterozygous transgenic hTau[AT] mice and maintained in culture for several weeks. Western blotting with pan-Tau antibody K9JA revealed a ~onefold overexpression in heterozygous slice cultures when compared to endogenous Tau levels (Fig 3A and B), well comparable with hippocampal extracts from adult hTau[AT] mice (Fig 1C). To detect the subcellular location of hTau[AT], we used immunohistochemistry with human Tau-specific antibody TauY9 or pan-Tau antibody K9JA. In slices from non-transgenic littermates, we could not detect any signal with antibody TauY9 (Fig 3C) but found an axonal distribution

Expression of hTau[AT] elevates intracellular Ca^{2+} concentrations in CA3 neurons at resting state and after membrane depolarization through NR2B-containing NMDA receptors

It was reported earlier that mis-sorted, phosphorylated Tau within dendritic spines of primary neurons impairs synaptic transmission by altering the densities of postsynaptic receptors such as AMPARs and NMDARs [12] and causes abnormal changes in intracellular Ca^{2+} ($[Ca^{2+}]_i$) [17]. We therefore investigated $[Ca^{2+}]_i$ by Fura-2AM imaging in organotypic hippocampal slices. Experiments were performed in area CA3 of slice cultures at DIV 15 (Fig 4A and B), when the NR2B to NR2A ratio in synapses is comparable to acute slices [31–33]. We observed a pronounced increase in resting $[Ca^{2+}]_i$ in hTau[AT] slices (~129 nM) compared to control littermate slices (~82 nM, Fig 4A–D). Next, slices were incubated and imaged for $[Ca^{2+}]_i$ in the presence of drugs to identify the source of the
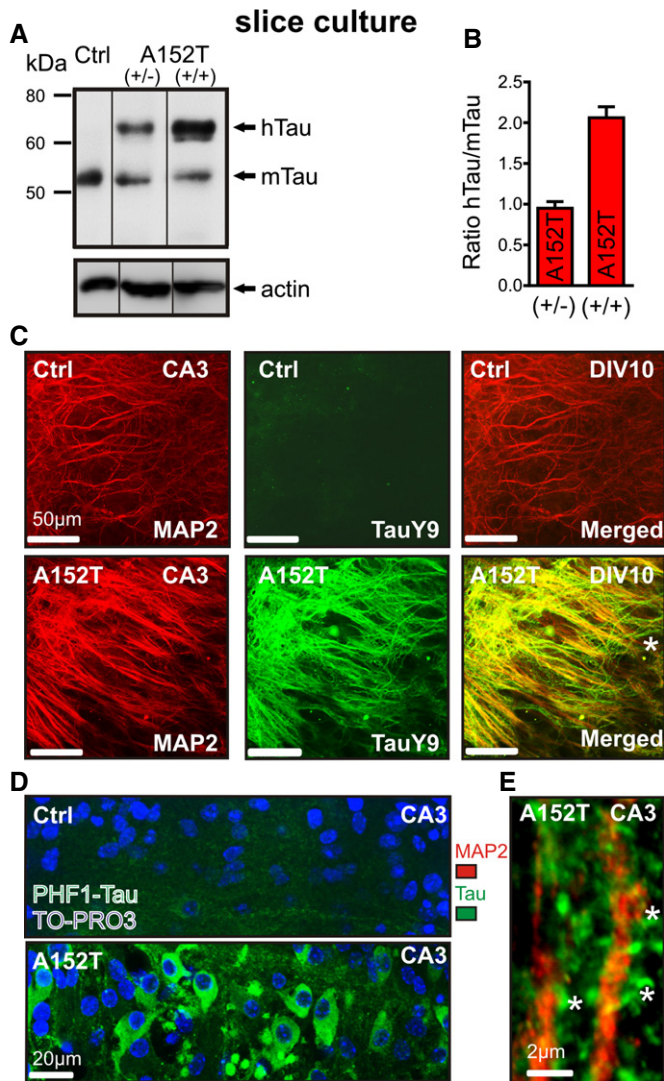
slice culture

Figure 3. hTau^AT expression causes Tau phosphorylation and mis-sorting in organotypic hippocampal slice cultures.

A   Western blot analysis with pan-Tau K9JA antibody to estimate expression levels of hTau^AT and endogenous Tau (mTau). Slice homogenates from non-transgenic littermate (lane 1, Ctrl), heterozygous hTau^AT (lane 2 (+/−)), or homozygous hTau^AT slices (lane 3 (+/+)) were analyzed after three weeks in culture. Actin served as a loading control.

B   Quantification of hTau^AT expression levels (n = average of 3–6 slice homogenates per group, error bars indicate mean ± SEM). The ratio between hTau^AT and endogenous mouse Tau is shown.

C   Immunohistochemistry with antibodies against human Tau (TauY9 antibodies; middle panel) and dendritic marker MAP2 (left panel) in slice cultures at DIV 10. Stratum radiatum of area CA3 is shown. Although MAP2 staining is apparent, no signal is detected by the TauY9 antibody in control slices. In contrast, in hTau^AT slices human Tau is detected in both dendrites and axons (see asterisk in merged image).

D   Immunohistochemistry against phosphorylated Tau at the PHF1 epitope in area CA3 of a control (upper lane) or hTau^AT slice (bottom lane). PHF1 staining is slightly visible in some axons in control slices. In contrast, PHF1-phosphorylated Tau is apparent in somata, dendrites and axons of neurons in hTau^AT slice cultures.

E   Higher magnification image of apical dendrites in area CA3 in a hTau^AT slice after immunohistochemistry against MAP2 (red) and Tau (K9JA antibody, green). Tau staining is seen in dendritic spines (asterisks) in contrast to MAP2, which is restricted to the dendritic shaft.

$[Ca^{2+}]_i$ increase. We applied the L-type voltage-gated calcium channel (L-VGCC) blocker nifedipine (NIF), the AMPAR antagonist CNQX, the NMDAR antagonists APV and ifenprodil (IFEN, inhibitor of NMDARs composed of NR1 and NR2B subunits [34]), memantine (MEM: preferentially blocking extrasynaptic NMDA receptor currents; [35]), the sodium channel blocker tetrodotoxin (TTX), and the presynaptic vesicle release inhibitor tetanus neurotoxin (TeNT), or imaged in the absence of extracellular Ca^{2+} (see Table EV1 for a summary of all drugs and concentrations used). In control littermate slices, the resting $[Ca^{2+}]_i$ was not significantly affected by these drugs (Fig 4D). However, as expected, the removal of extracellular Ca^{2+} leads to a pronounced decrease in $[Ca^{2+}]_i$ (−50%, ~40 nM, $P < 0.05$, Fig 4D). In agreement, Ca^{2+}-free saline caused the strongest $[Ca^{2+}]_i$ reduction in hTau^AT slices (−55%, ~55 nM, $P < 0.0001$, Fig 4D) but additionally the blockade of NMDAR with APV leads to a reduction in resting $[Ca^{2+}]_i$ (~83.5 nM, $P < 0.05$, Fig 4D).

The inhibition of extrasynaptic NMDARs (either by IFEN or by low-dose MEM) or the blockage of L-VGCC (by NIF) was sufficient to reduce resting $[Ca^{2+}]_i$ in hTau^AT-expressing slices to control levels (IFEN: ~70 nM, $P < 0.05$; MEM: ~83 nM, $P < 0.01$; NIF: ~83 nM, $P < 0.05$, Fig 4D). $[Ca^{2+}]_i$ levels were not significantly altered in presence of either TTX, TeNT, or CNQX in both control and hTau^AT slices under resting conditions (Fig 4D).

Next, changes in calcium influx after membrane depolarization were monitored by applying high potassium chloride (KCl). After activity induction, we observed a steep rise in $[Ca^{2+}]_i$ levels in hTau^AT slices (~575 nM, Fig 4E), whereas control slices achieved only maximum values of ~300 nM (Fig 4E). KCl-evoked Ca^{2+} influx was blocked by nifedipine (NIF: −47%, $P < 0.05$, Fig 4E) and less prominently by APV (−36%, Fig 4E) in control littermate slices.

In contrast, treatment of hTau^AT slices with APV caused a stronger inhibition of Ca^{2+} influx than application of NIF (−56%, $P < 0.001$; APV: −69%, $P < 0.001$, Fig 4E).

Comparison of the effects of MEM and IFEN on KCl-evoked Ca^{2+} influx in control (MEM: −1%; IFEN: −13%, Fig 4E) and in hTau^AT slices (MEM: −44%, $P < 0.05$; IFEN: −48%, $P < 0.01$, Fig 4E) demonstrated a prominent contribution of NR2B-mediated Ca^{2+} influx to the overall $[Ca^{2+}]_i$ increase in hTau^AT slices.

hTau^AT expression is neurotoxic by increasing extracellular glutamate, thereby activating the CREB shutoff pathway

Adult excitatory neurons of the hippocampus express NMDARs with mainly two subunit compositions, NR1/NR2A and NR1/NR2B [36,37]. Synaptic NMDARs are predominantly of the types NR1/NR2A or NR1/NR2A/NR2B (ifenprodil insensitive), whereas somatic or extrasynaptic NMDARs are predominantly of the type NR1/NR2B (ifenprodil sensitive) [36]. The pathway downstream of NMDAR activation is dependent both on the subunit composition and on the location of the receptors [38,39]. For example, Ca^{2+} flux through synaptic NMDARs initiates changes in synaptic efficacy and promotes pro-survival events, whereas Ca^{2+} flux through extrasynaptic NMDARs is coupled to cell-death pathways [38,40,41]. The pharmacology of calcium imaging experiments (IFEN, MEM) pointed to a strong contribution of NR2B-containing extrasynaptic
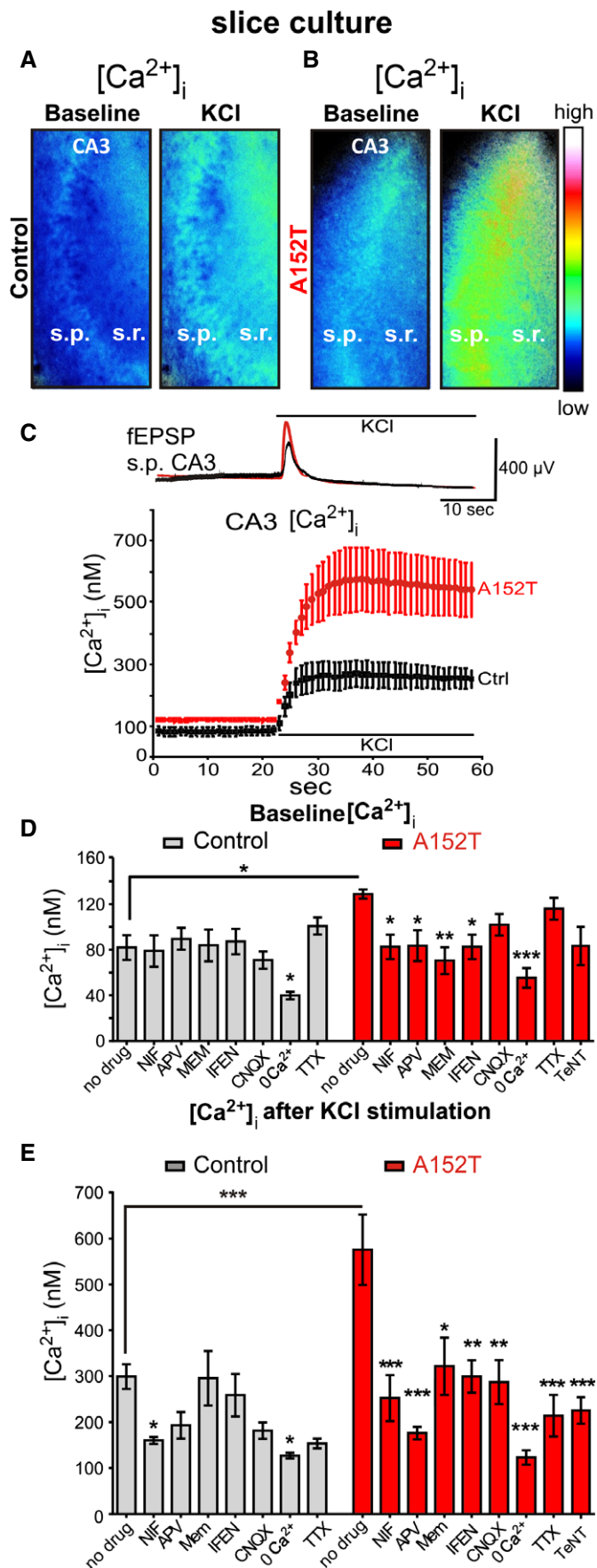
Figure 4. hTau[AT] causes elevation of Ca^{2+} levels in CA3 hippocampal neurons at resting state and after membrane depolarization through extrasynaptic NMDA receptors.

A   Slices (DIV 15) from control mice were loaded with the Ca^{2+}-sensitive dye Fura-2AM. Ratiometric images are presented at baseline and after application of high potassium. Note the increase in intracellular Ca^{2+} ([Ca^{2+}]$_i$) after KCl application.

B   Slices (DIV 15) from hTau[AT] mice were loaded with the Ca^{2+}-sensitive dye Fura-2AM. Ratiometric images at baseline and after application of high potassium chloride in area CA3 are depicted. Note the increase in [Ca^{2+}]$_i$ (false color legend) under both conditions in hTau[AT] slices compared to controls.

C   Electrophysiological example traces (control, black; hTau[AT], red) of excitatory postsynaptic field potentials (fEPSP) depict examples of depolarizations that are induced by a single high potassium chloride application in stratum pyramidale (s.p.) of area CA3 in slices in which calcium imaging experiments were conducted. The example depolarization evokes averaged calcium influxes into neurons depicted in the calcium imaging graph. The graph shows the mean of [Ca^{2+}]$_i$ changes in response to high KCl in stratum radiatum and stratum pyramidale of area CA3 in Fura-2AM-loaded hippocampal slices. After depolarization, [Ca^{2+}]$_i$ rises up to ~600 nM in hTau[AT] slices (red trace, $n = 6$ slices, prepared from at least three animals), compared to ~300 nM in control slices (black trace, $n = 6$ slices; prepared from at least three animals). Note that even under resting conditions, [Ca^{2+}]$_i$ is elevated to ~120 nM due to hTau[AT] expression.

D   Quantification of the [Ca^{2+}]$_i$ from ratiometric images as depicted in (A) and (B) after background subtraction and selection of regions of interest (10 circles of fixed diameter) in stratum radiatum border to stratum pyramidale of area CA3. Under resting conditions, [Ca^{2+}]$_i$ was elevated in transgenic slice cultures (~120 nM, $n = 11$) compared to controls (~80 nM, $n = 8$). Slices were incubated with one of the following channel blockers: nifedipine (NIF, VGCC; Ctrl $n = 8$; A152T: $n = 7$), APV (NMDAR; Ctrl $n = 7$; A152T $n = 8$), ifenprodil (IFEN, NMDAR; Ctrl $n = 8$; A152T $n = 7$), memantine (MEM, NMDAR; Ctrl/A152T $n = 6$), 6-cyano-7-nitroquinoxaline-2,3-dione (CNQX; AMPAR; Ctrl $n = 8$; A152T $n = 7$), tetrodotoxin (TTX, VGNaC; Ctrl $n = 4$; A152T $n = 5$), tetanus neurotoxin (TeNT, neurotransmitter release; A152T $n = 6$) or in Ca^{2+}-free buffer (Ctrl $n = 10$; A152T $n = 7$). For each experiment, slice preparations from at least three different mice were used. One-way ANOVA followed by Tukey's *post hoc* test; Ctrl: $F(7/51) = 3,533$; $P = 0.0036$; A152T: $F(8/55) = 5,230$; $P < 0.0001$. For an overview of drug concentrations see Table EV1.
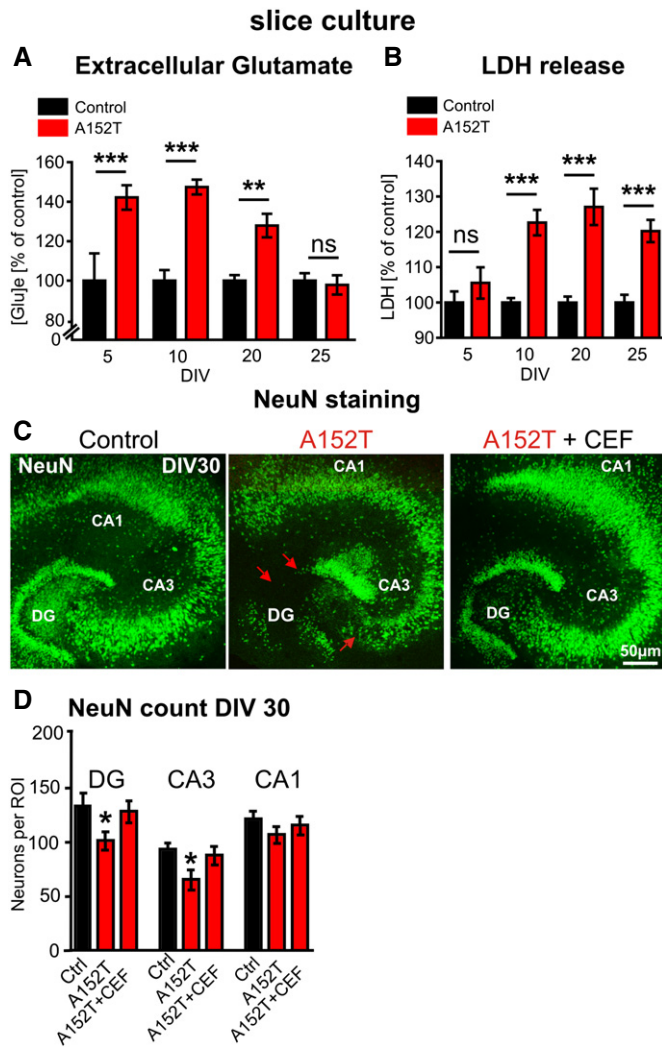
E   Quantification of the maximum peak increase in intracellular calcium after high KCl stimulation. One-way ANOVA followed by Tukey's *post hoc* test Ctrl: $F(7/45) = 4,080$; $P = 0.0015$; A152T: $F(8/53) = 7,580$; $P < 0.0001$).

Data information: Error bars represent SEM; one-way ANOVA: *$P < 0.05$, **$P < 0.01$, ***$P < 0.001$.

NMDARs under both conditions, resting and activity-induced Ca^{2+} influx in hTau[AT] slices, not seen in control littermate slices.

Since NR2B-containing NMDARs get activated by excessive glutamate [42], we hypothesized the possibility of high levels of extracellular glutamate in hTau[AT] slices. To test this, culture medium from hTau[AT]-expressing (or control littermate) slices was collected at different time points and glutamate concentrations were measured. The extracellular glutamate levels from hTau[AT] slices were increased by ~45% at DIV 5 and DIV 10 and declined at DIV 20–25 almost to control levels (+28% (DIV 20) and −4% (DIV 25); Fig 5A). The maximum glutamate concentrations were already observed at early time points (DIV 5 and 10; Fig 5A). Remarkably, the increase in glutamate was already maximal several days before the increase in cytotoxicity as seen by LDH (Fig 5B), which argues in favor of a rise in extracellular glutamate as a trigger for toxicity.

To test whether augmented, NR2B-mediated calcium influx in hTau[AT] slices leads to downstream cell-death signaling pathway, we

slice culture

Figure 5. hTau[AT] expression enhances extracellular glutamate, cytotoxicity and progressive neuronal loss in the hippocampus.

A   Glutamate content in the culture medium ([Glu]$_e$) from either hTau[AT] (*n* = 10 culture inserts containing 6 slices each) or control slices (*n* = 5–12 culture inserts) analyzed at DIV 5, 10, 20 and 25. Glutamate content from medium cultured with hTau[AT] slices is shown in percent of control at each time point. Increased levels were observed between DIV 5 and DIV 20. At DIV 25, glutamate levels already declined to control levels. One-way ANOVA followed by Tukey's *post hoc* test: **$P < 0.01$, ***$P < 0.001$.

B   Lactate dehydrogenase (LDH) release (a measure of cytotoxicity) analyzed in hTau[AT] (*n* = 17–19 culture inserts containing 6 slices each) or control slices (*n* = 15–16 culture inserts) at DIV5, 10, 20 and 25. LDH release of hTau[AT] slices is shown in percent of control at each time point. A pronounced increase (~25%) in LDH release was observed due to hTau[AT] expression starting at DIV 10 but not at DIV 5. One-way ANOVA; ***$P < 0.001$.

C   Slice cultures from control (left), hTau[AT] (middle) or hTau[AT] treated with ceftriaxone (CEF 100 μM; right) stained against neuronal nuclear protein (NeuN) at DIV 30. Representative neuronal cell layers are shown. hTau[AT] slices show neuronal loss in the granular cell layer of the dentate gyrus and the pyramidal cell layer in the region of the hilus in area CA3 (middle panel, red arrows). Treatment with ceftriaxone for 30 days prevents neuronal loss in DG and area CA3.

D   NeuN-positive cell bodies were counted in the DG and within the pyramidal cell layer in area CA3 and CA1 at DIV 30 in defined regions of interest (ROI). The number of neurons was reduced in hTau[AT] slices, both within area DG and CA3, whereas the number of neurons in the CA1 was only slightly affected. Neuronal loss was largely prevented in cultures treated with ceftriaxone (CEF) in dentate gyrus and area CA3 (*n* = 14–19 slices per group and area; prepared from at least 6 animals). One-way ANOVA followed by Tukey's *post hoc* test; *$P < 0.05$.

Data information: Error bars represent mean ± SEM.

evaluated the effect of hTau[AT] on cytotoxicity. This revealed an increase in lactate dehydrogenase (LDH) release, a marker for dying cells, starting at DIV 10 (+23%; Fig 5B) and lasting over the whole cultivation period of 25 days (+27% at DIV 20, +20% at DIV 25; Fig 5B). An exception was the earliest time point of measurement (DIV 5) where toxicity stayed close to control levels (+5%, Fig 5B), demonstrating that toxicity progresses from young to older hTau[AT] slices. The question therefore arose, what is the cause of the rise in Ca^{2+} and of cytotoxicity in slices from hTau[AT] mice?

To further differentiate between cytotoxicity and neurotoxicity and to test a possible differential vulnerability of hippocampal subregions, NeuN immunohistochemistry was performed. NeuN-expressing cells were counted at DIV 30 and showed a selective neuronal loss in area CA3 (−30%, *P* = 0.015) and DG (−23%, *P* = 0.032, Fig 5C and D) in hTau[AT]-expressing slices, whereas CA1 neurons were only mildly affected (−11%, *P* = 0.15, Fig 5D). We further analyzed neurons in slices at an earlier (DIV 10; Fig EV2A) and a later time point (DIV 60; Fig EV2B). At DIV 10, no significant cell loss was detected in areas DG, CA1, and CA3. In contrast, at DIV 60 neuronal loss was even more pronounced when compared to values observed at DIV 30. These findings in slice cultures were supported by the observation of neuronal cell loss in the

hippocampus of aged hTau[AT] mice. Neuronal cell loss was prominent in the pyramidal layer of area CA3 in 12-month-old heterozygous hTau[AT] mice (Fig EV5A). Next, we analyzed NeuN protein levels in hippocampi of 12- and 18-month-old hTau[AT] mice (Fig EV5B and C). Here, we found a progressive loss of NeuN expression which was reduced by ~10% already in 12-month-old hTau[AT] mice and neuronal loss became more pronounced to ~35% in 18-month-old hTau[AT] mice when compared to control mice (Fig EV5B and C). Hippocampal neurotoxicity was also confirmed in hippocampi from 16-month-old, heterozygous hTau[AT] animals by quantitative real-time PCR. NeuN mRNA was significantly decreased in hippocampi from hTau[AT] mice compared to control littermate hippocampi (*n* = 4 animals per group, unpaired *t*-test: *P* = 0.0323, Fig EV2C). The activity of the pro-apoptotic caspase 3 was not increased in hTau[AT] slices compared to control (*P* = 0.4143; Fig EV2D). This points to a necrotic caspase-independent pathway rather than apoptotic events leading to neuronal cell death.

Ca^{2+} flux through extrasynaptic NMDARs is known to induce dephosphorylation of CREB protein (at Ser133) which in turn causes shut-off of the CREB pathway, leading to neuronal death [38,40,43]. Therefore, we monitored a potential CREB shut-off in hTau[AT] slices by Western blot analysis for total CREB and pS133-CREB (Fig EV2E). There was a marked reduction (−50%; *P* = 0.0064) in active pCREB levels in the mutant slices (Fig EV2E). Taking these findings together with the elevated levels of extracellular glutamate and elevated [Ca^{2+}]$_i$, we conclude that a pathological increase in Ca^{2+} influx through extrasynaptic NMDARs takes place in hTau[AT] slices resulting in

activation of the pro-death CREB shut-off pathway and subsequent neurotoxicity.

The hTau[AT] mutation enhances synaptic transmission and susceptibility for epileptiform activity in area CA3 without affecting synaptic plasticity

The shut-off of CREB activity influences not only synaptic plasticity and memory formation but also neuronal survival [44] which is based on the proper function of dendritic spines [45]. We thus analyzed dendritic spine density of 10- to 12-month-old, heterozygous hTau[AT] mice. Apical dendrites of hTau[AT] CA3

pyramidal neurons displayed a 50% increased spine density compared to control littermate animals (2.04 ± 0.15 spines/μm and 1.36 ± 0.05 spines/μm, $P = 0.039$; Fig 6A–C). In organotypical slices at DIV 20, the spine density of CA3 apical dendrites was unchanged in hTau[AT] slices (control: ~1.6 spines, hTau[AT]: ~1.4 spines/μm, Fig EV3A–E).

Long-term potentiation (LTP) is a common way to measure learning and memory on a cellular scale because memories are encoded by changes in synaptic strength through LTP and LTD [46]. We used excitatory postsynaptic field potentials (fEPSP) in stratum lucidum of area CA3 to measure basal synaptic transmission, short-term plasticity and long-term plasticity of the mossy fiber pathway,
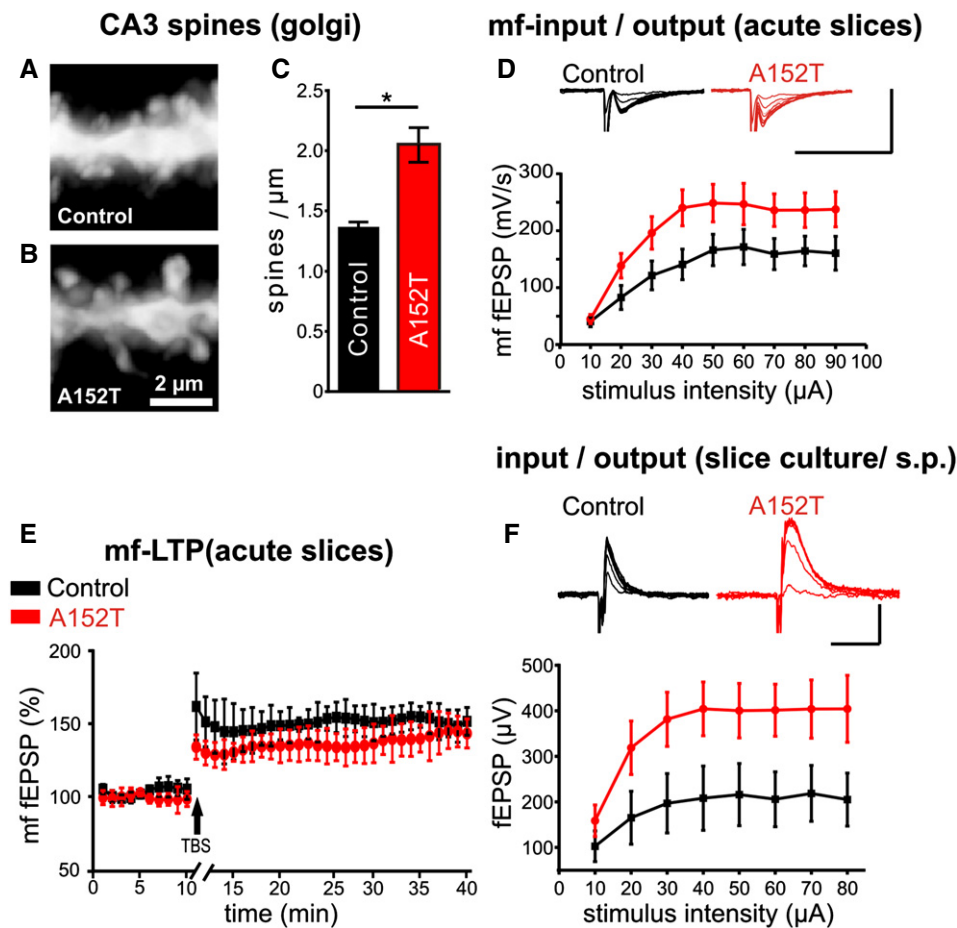

Figure 6. hTau[AT] enhances synaptic transmission and dendritic spine density in area CA3 but does not interfere with synaptic plasticity.

A   Representative microphotograph of spines on dendrites from control littermate mice at the age of 12 months. Apical dendrites from CA3 pyramidal neurons are visualized by Golgi staining. The contrast of photomicrographs was inverted.
B   Dendritic spines from heterozygous hTau[AT] mice, seen by Golgi staining.
C   Quantification of dendritic spine densities in control littermate and hTau[AT] mice. Note that the spine density in heterozygous hTau[AT] is increased (control littermates: $n = 2$ animals; heterozygous hTau[AT]: $n = 4$ animals; an average of 5 dendrites of CA3 pyramidal neurons were analyzed per animal; unpaired *t*-test).
D   Input/output curve of field potential recording in the mossy fiber pathway in acute slices of $12(\pm 1)$-month-old mice demonstrating significantly enhanced basal synaptic transmission (multiple repeat ANOVA, $F(9, 126) = 2.00$, $P = 0.044$) in area CA3 in mice expressing hTau[AT]. Scale bars: 500 μV vertical bar and 20 msec horizontal bar.
E   Long-term potentiation in the mossy fiber pathway demonstrates no differences in long-term plasticity between control (black) and hTau[AT]-expressing mice (red).
F   Input/output curve of field potential recording in stratum pyramidale (s.p.) of area CA3 in organotypic hippocampal slices at DIV 30. Somatic field potentials are increased in hTau[AT] compared to control littermates. Scale bars: 800 μV vertical bar and 20 msec horizontal bar.

Data information: Error bars represent SEM; *t*-test: *$P < 0.05$.

since this pathway was found to be particularly affected as judged by tauopathy markers (e.g., PHF1, Alz-50, Figs 1 and 2). Recording input/output curves of the mossy fiber pathway from $12(\pm1)$-month-old hTau^{AT} ($+/-$) mice revealed an increase in basal synaptic transmission compared to non-transgenic siblings (Fig 6D). At 10 μA stimulation intensity, fEPSP responses still stayed at the same level in control littermates and hTau^{AT} animals (40.4 ± 9.1 mV/s, $n = 7$ and 44.8 ± 8 mV/s, $n = 9$; Fig 6D), but when comparing all other stimulation intensity steps the responses of hTau^{AT} mice were clearly increased. The maximum of the i/o curve of hTau^{AT} animals was reached at 50 μA stimulation intensity (248.49 ± 33.1 mV/s, $n = 9$; Fig 6D), whereas control littermates reached the maximum fEPSP only at 60 μA stimulation intensity (171.4 ± 30.9 mV/s, $n = 7$; Fig 6D). However, short-term plasticity (paired-pulse facilitation) remained unaffected in hTau^{AT} mice (paired-pulse ratio control littermates: 1.44 ± 0.08, $n = 31$ and hTau^{AT}: 1.48 ± 0.05, $n = 33$; Fig EV3F). The same was true for long-term plasticity evoked by theta burst stimulation in the mossy fiber pathway. There were no differences in the level of potentiation of the last 10 min of LTP recording (control littermates: $152 \pm 9.7\%$ of baseline, $n = 6$ and hTau^{AT}: $141.2 \pm 12.2\%$ of baseline, last 10 min of recording, $n = 7$; Fig 6E).

Similar to the situation in acute hippocampal slices, recording evoked fEPSPs in stratum pyramidale of area CA3 in DIV 26–30 old hTau^{AT} organotypic slices revealed elevated amplitudes of somatic fEPSPs in stratum pyramidale (Fig 6F). At an input stimulus intensity of 10 μA, the average output fEPSP amplitude in control littermate slices was 102.5 ± 33.64 μV ($n = 5$) and 158.58 ± 34.79 μV ($n = 15$) in hTau^{AT} slices; however, overall amplitudes were increased in hTau^{AT} slices compared to control littermates (multiple repeat ANOVA, $F(7,89) = 2.1874$, $P = 0.042$; Fig 6F). In younger slices at DIV 10, this effect was not observed (no significant difference between control ($n = 5$) and hTau^{AT} slices ($n = 12$); multiple repeat ANOVA, $F(7,77) = 1.1472$, $P = 0.34$, Fig EV3G), which suggest a progression of this phenotype with age.

Given that basal synaptic transmission in the mossy fiber tract of hTau^{AT} mice was increased, we hypothesized that this might be accompanied by elevated susceptibility for epileptiform activity. To investigate this, we recorded field potentials (fEPSPs) in stratum pyramidale of area CA3 in hTau^{AT}-expressing slices. Picrotoxin (50 μm) was used to induce epileptiform discharges by blocking GABAergic transmission in control slices and hTau^{AT}-expressing slices at two time points (DIV 10 and DIV 30). After washing in picrotoxin diluted in ACSF, recurrent epileptiform discharges occurred approximately after 3 min (Fig 7A and B). At DIV 10, when extracellular glutamate concentrations are enhanced in hTau^{AT} slices (Fig 5B), we observed an increase in burst frequency (bursts per minute) compared to control littermate slices (control: 1.07 ± 0.21 burst per minute, $n = 8$ slices and hTau^{AT}: 1.82 ± 0.169 bursts per minute, $n = 8$, two-sample t-test: $P = 0.001$; Fig 7C). In addition, the number of firings per burst was enhanced by ~40% (control: 5.80 ± 0.73 firings per burst, $n = 7$ slices and hTau^{AT}: 8.32 ± 0.41 firings per burst, $n = 5$; two-sample t-test: $P = 0.004$; Fig 7D). Recording at a later time point (DIV 30), when excessive extracellular glutamate levels drop down to control levels (Fig 5A), demonstrated that enhanced epileptiform activity becomes even more pronounced. At this time point, hTau^{AT}-expressing slices display on average 2.56 ± 0.26 bursts per minute ($n = 10$, Fig 7E)

after picrotoxin wash-in, which was ~100% higher than recorded in control littermate slices (1.24 ± 0.37 bursts per minute, $n = 5$, two-sample t-test: $P = 0.006$; Fig 7E).

Applying the β-lactam antibiotic ceftriaxone (CEF), which is known to upregulate the astrocytic excitatory amino acid transporter EAAT2/GLT1 expression and its biochemical activity [47], prevented the burst frequency increase in hTau^{AT} slices, presumably by normalizing extracellular glutamate levels (1.74 ± 0.35 bursts per minute, $n = 5$, Fig 7E). Similar to the burst frequency, firings per burst were strongly enhanced (~80%) at DIV 30 in slices expressing hTau^{AT} (control: 4.47 ± 0.42 firings per burst, $n = 5$ and hTau^{AT}: 8.74 ± 0.45, $n = 10$, Fig 7F, t-test: $P = 0.0000001$). Finally, a pathological change in slices expressing hTau^{AT} recorded at DIV 30 was prevented by ceftriaxone (4.71 ± 0.32 firings per burst, $n = 6$, Fig 7F).

Staining by pan-Tau antibody (K9JA) indicated that hTau^{AT} slices used for epileptiform activity recordings displayed increased mossy fiber sprouting (Fig 7G and H). In adult heterozygous A152T mice, we confirmed network hyperactivity in the hippocampus by a significant increase in c-Fos mRNA expression in comparison to control littermates ($n = 4$ animals per group, $P = 0.001$, Fig EV4A). c-Fos is upregulated in the hippocampus under a variety of activity inducing conditions, for example, seizure induction [48]. At the same time, Homer1a was downregulated (Fig EV4B) in such animals pointing to a disturbed Homer scaffolding with metabotropic glutamate receptors, which is causative for an epileptic phenotype in a mouse model with fragile X syndrome [49,50]. However, we did not observe any changes in transcription levels of NR2B and NR2A receptors (Fig EV4C and D).

Enhanced presynaptic glutamate release is responsible for excitotoxicity due to hTau^{AT} expression

The observation that extracellular glutamate concentrations are elevated even before cytotoxicity becomes enhanced (Fig 5A and B) was indicative of a mechanism of glutamate-mediated excitotoxicity in hTau^{AT} slices. To prove that excess glutamate in the slice medium was due to enhanced neuronal activity (causing elevated neurotransmitter release), we next incubated the slices with either tetrodotoxin (TTX: 1 μM) to inhibit action potentials driven by voltage-gated sodium channels or tetanus neurotoxin (TeNT: 50 nM) to inhibit glutamate release from presynaptic terminals. In both conditions, glutamate levels in hTau^{AT} slices dropped down to control levels (TeNT: -57%; TTX: -35%; Fig 8A). Both inhibitors had smaller effects in control slices (TeNT: -35%; TTX: -25%; Fig 8A), indicating that elevated glutamate levels are due to hTau^{AT} expression.

EAAT2/GLT1 plays important roles in restricting extracellular glutamate concentrations in order to limit the activation of glutamate receptors, thereby protecting neurons from excitotoxicity [51]. To test this, EAAT2/GLT1 was blocked by treating slices with benzyloxyaspartic acid (TBOA, 50 μM). This caused a strong increase in glutamate in control slices ($+66\%$; $P < 0.01$), but only a small rise in hTau^{AT} slices ($+24\%$, Fig 8B) accompanied by an increase in cytotoxicity (LDH; control: $+50\%$; $P < 0.001$; hTau^{AT}: $+28\%$, $P < 0.001$, Fig 8C).

To investigate mechanisms causing the rise in extracellular glutamate due to hTau^{AT} expression, we treated organotypic cultures
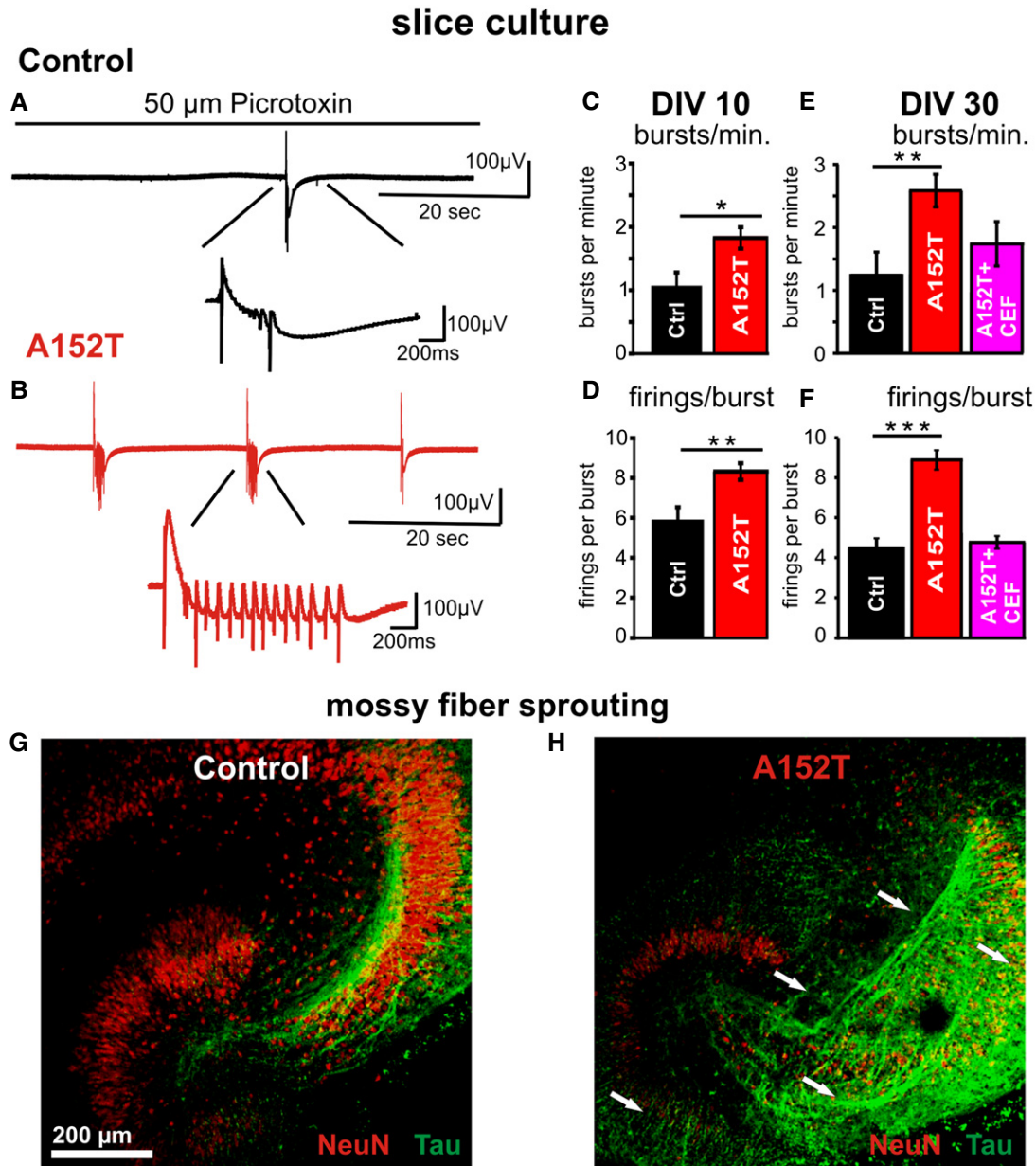
Figure 7. 2Cultured slices expressing hTau[AT] show a progressive increase in epileptiform activity and mossy fiber sprouting which can be prevented by CEF application.

A   Example of electrophysiological fEPSP recording in stratum pyramidale of area CA3 in a control slice (DIV 30) during wash-in of 50 μM picrotoxin. This leads to blockage of GABAergic transmission followed by epileptiform discharges (burst) occurring approximately after 3 min. The zoom-in reveals that such an epileptiform discharge (burst) consists of repetitive firings.

B   Similar example trace as in (A) recorded in a hTau[AT]-expressing slice (red) demonstrating an increase in burst frequency as well as in firings per burst due to hTau[AT] expression.

C   Quantification of bursts per minute in DIV 10 slices from control littermates and hTau[AT] slices demonstrating a ~twofold increase in hTau[AT] slices (*n* = 8 slices per group).

D   Firings per burst are increased ~1.5-fold already at the early time point DIV 10 due to hTau[AT] expression.

E   Analysis of burst frequency in slices at DIV 30 demonstrates the progression of the pathological effect beyond that observed at DIV 10. Burst frequency is enhanced in hTau[AT]-expressing slices (*n* = 10 slices). If ceftriaxone (CEF) is applied to hTau[AT] slices, the pathological burst frequency enhancement is partly prevented (*n* = 5 slices).

F   Firings per burst are strongly enhanced due to hTau[AT] expression in slices at DIV 30. Ceftriaxone prevents this pathological phenotype if applied during the entire period of cultivation (*n* = 6 slices).

G   Example of a control littermate organotypic slice culture at DIV 24 stained against NeuN (red) and pan-Tau (K9JA antibody, green). Axonal projections (green) of granule cells (red) in the dentate gyrus are depicted.

H   Hippocampal slice culture expressing hTau[AT] stained against NeuN (red) and pan-Tau (green) showing mossy fiber sprouting in the hilar region, CA3 and dentate gyrus (white arrows).

Data information: Error bars represent SEM; *t*-test: *P < 0.05, **P < 0.01, ***P < 0.001.
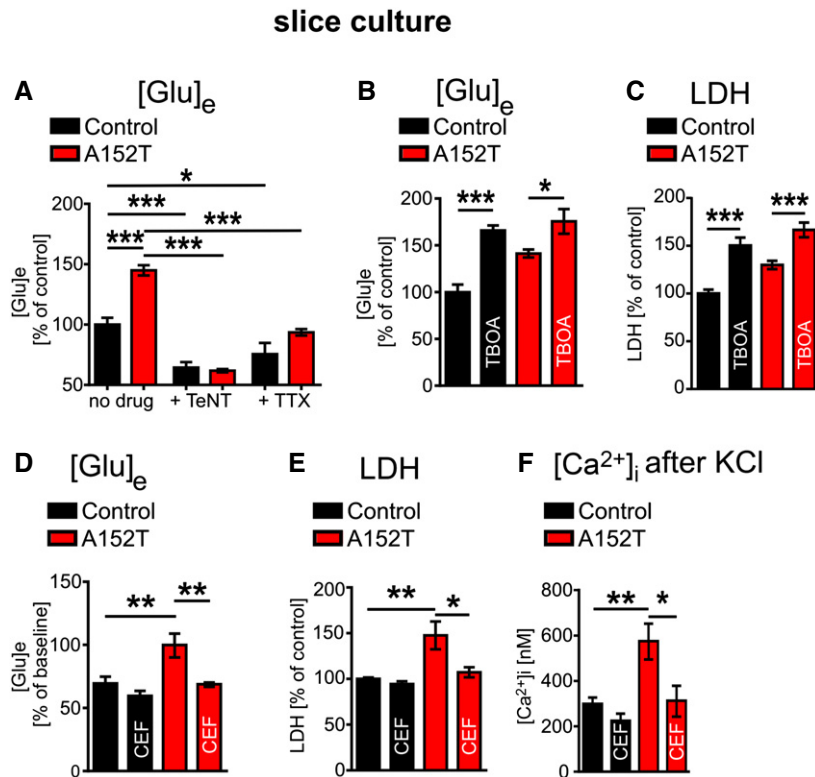
slice culture

Figure 8. The pathophysiological phenotype of hTau[AT] expression is related to enhanced presynaptic release and is prevented by increasing EAAT2/GLT1 activity.

A Quantification of glutamate concentrations in the medium of control and hTau[AT] cultures in the presence of either 50 nM tetanus neurotoxin (TeNT) or 1 μM tetrodotoxin (TTX) at DIV5. Under both conditions, glutamate levels in the culture medium of hTau[AT] slices decreased to control levels (*n* = 6 culture inserts containing 6 slices each/group and condition).

B Quantification of extracellular glutamate concentrations in culture medium of either control or hTau[AT] slices at DIV 20 in the presence or absence of 50 μM benzyloxy-aspartic acid (TBOA) from DIV 1-DIV 20 demonstrating a possible contribution of astrocytic glutamate dysregulation to increased extracellular glutamate in hTau[AT] slices (*n* = 8–9 culture inserts containing 6 slices each/group and condition). One-way ANOVA $F_{(3,30)}$ = 14,89; $P < 0.001$.

C Quantification of LDH release into the culture medium of either control or hTau[AT] slices at DIV 20 in the presence or absence of 50 μM benzyloxy-aspartic acid (TBOA) from DIV 1 to DIV 20 (*n* = 6–12 culture inserts containing 6 slices each/group and condition). One-way ANOVA followed by Tukey's *post hoc* test.

D Quantification of extracellular glutamate concentrations in either control or hTau[AT] cultures (*n* = 7–8 culture inserts containing 6 slices each/group and condition) treated with ceftriaxone from DIV 1 to DIV 25 demonstrating the preventative effect of CEF on the increase in extracellular glutamate in hTau[AT] slices. One-way ANOVA $F_{(3,25)}$ = 9.075; $P = 0.0003$.

E LDH release at DIV 25 is strongly reduced due to long-term treatment with ceftriaxone in hTau[AT] slice cultures (*n* = 8–10 culture inserts containing 6 slices each/group and condition). One-way ANOVA $F_{(3,32)}$ = 7.685; $P = 0.0005$.

F Intracellular calcium rise after KCl stimulation is not distinguishable from control slices in hTau[AT] slices treated with ceftriaxone for 15 days (*n* = 5–9 slices; prepared from at least three animals). One-way ANOVA $F_{(3,25)}$ = 7.317; $P = 0.0011$.

Data information: Error bars represent SEM; one-way ANOVA followed by Tukey's *post hoc* test: *$P < 0.05$, **$P < 0.01$, ***$P < 0.001$.

with ceftriaxone (CEF: 100 μM, starting at DIV 1) (Figs 8D–F and 5C and D). Indeed, treatment with CEF prevented all pathological phenotypes in hTau[AT]-expressing slices mentioned above, that is, (i) extracellular glutamate (Fig 8D), (ii) maximum calcium influx after membrane depolarization (Fig 8F), (iii) neurotoxicity measured by LDH release (Fig 8E), (iv) epileptiform activity (Fig 7E and F), and (v) neuronal loss (by NeuN counting; Fig 5C and D).

Discussion

In the present study, we used aged hTau[AT] mice and organotypic hippocampal slices from P8 mice to characterize the pathophysiological phenotype of the recently described Tau mutation p.A152T

[4,7]. This mutation is a risk factor for FTD-spectrum disorders such as PSP or CBD, and AD. However, its pathogenic effects are poorly understood. In transgenic mice and slice cultures, we found characteristic signs of Tau pathology, that is, phosphorylation, pathological conformation, somato-dendritic mis-sorting, aggregation, neuronal degeneration, and loss due to hTau[AT] expression, similar to human carriers [5,6]. The slices revealed a remarkable increase in intracellular Ca^{2+} concentration in hippocampal CA3 neurons, both at resting state and after membrane depolarization. These alterations were apparent before Tau aggregates, suggesting oligomeric forms of Tau as mediators of these changes. Indeed, *in vitro* experiments had shown that p.A152T favors the formation of oligomers [7]. This is remarkable because the mutation lies in the N-terminal domain, far away from the repeat domain that forms the core of aggregation, and

therefore, one would not expect the mutation to have an effect on tau aggregation.

To identify the origin of the intracellular Ca^{2+} increase, we tested different drugs and found that intracellular Ca^{2+} concentrations were normalized by ifenprodil and memantine (targeting NR2B-containing NMDA receptors) but also by nifedipine (targeting VGCCs). Since we also observed enhanced extracellular glutamate levels in hTau^{AT} slices, we assume this phenotype to cause network hyperactivity. This was confirmed by the measurements of epileptiform activity. In conclusion, an increased network activity could lead to constant enhancement of extracellular glutamate concentrations, which would in turn lead to increased NR2B activation causing increased intracellular Ca^{2+} concentrations.

For future investigation, it would be worth investigating whether a Na/Ca exchanger reversal is contributing to the high intracellular calcium concentration comparable to the situation in other excitotoxic phenotypes (e.g., ischemia, stroke). Since we found no indication of disturbances in NR2A or NR2B transcription by real-time PCR measurements (Fig EV4C and D), one can speculate that the enhanced calcium influx through NR2B-containing NMDAR at resting state should be due to receptor/channel dysfunction caused by somato-dendritic mis-sorted Tau. Indeed, we observed enhanced epileptiform activity in hTau^{AT} slices at DIV 10 and 30 as well as an increase in synaptic transmission. Consistent with this, several reports have suggested the involvement of the NR2B subunit in the mediation of seizures [52], and the reduction in Tau leads to seizure resistance in epilepsy models [21,53]. Moreover, when rats were treated with transient middle cerebral artery occlusion to initiate an excitotoxic insult, NR2B-containing NMDARs were overactivated, resulting in Tau hyperphosphorylation and aggregation [54].

It is notable that different Tau mutations may have opposite consequences on synaptic transmission in mice: Pro-aggregant mutations in Tau's repeat domain (Δ280) lead to reduced transmission in the mossy fiber tract [15,55,56], whereas the amino-terminal mutation A152T, described here, enhances transmission in the same pathway. By analogy, there can be opposite effects in terms of calcium levels, which are reduced in neurons expressing Tau^{RDΔK280} [15,16] and increased when A152T Tau is expressed. Enhanced calcium levels were also observed in SH-SY5Y cells expressing Tau with a V337M mutation [57]. EEG studies of human hTau^{AT} carriers are not available so far, but increased seizure susceptibility was described for PSP [26] and Alzheimer's disease patients [58].

Notably, we did not observe any changes in synaptic plasticity of the CA3 synapses but an increase in spine density of CA3 pyramidal neurons. An increase in spine density is also observed under excitotoxic conditions in animals which have undergone transient global ischemia [59]. This is in strong contrast to mouse models expressing Tau with mutations in the repeat domain which show reduced plasticity and synapse loss [14,55,56].

The CREB shut-off pathway is well established, assuming that enhanced intracellular calcium concentrations through NR2B-containing NMDAR lead to necrotic cell death [38]. In agreement with this pathway, we observed a decreased ratio of phospho-CREB/CREB, at the same time no alteration in caspase-3 activity but progressive neuronal cell death due to hTau^{AT} expression in organotypic slices and in adult animals. This correlates well with the observation of enhanced glutamate content in the slice medium of hTau^{AT} slices. Elevated levels of glutamate cause excitotoxic insults which finally lead to neurotoxicity [60]. The strongest vulnerability was seen in the DG and CA3, the same regions that were affected in aged hTau^{AT} mice by enhanced synaptic transmission in acute slices as well as in organotypic slices and by increased epileptiform activity in organotypic slices. Moreover, in cultured slices we observed mossy fiber sprouting demonstrating this pathway to be severely affected during the process of pathogenesis. At the ultrastructural level, degenerative hallmarks were observed in aged transgenic mice by electron microscopy in the somato-dendritic compartment as well as in axons.

It is interesting to compare our results with those of Mucke and colleagues who created regulatable transgenic mice with the same mutation (A152T), but in a different human Tau isoform (1N4R), and under a different promoter, CaMKII-tTA [27]. These mice developed a comparable phenotype including age-dependent neuronal loss and spontaneous nonconvulsive epileptiform activity. Tau pathology markers and neuronal loss were most prominently found in hippocampal areas CA3 and DG; however, synaptic plasticity was not affected in both mouse lines. The similarity of phenotypes argues for a common pathway of toxicity induced by the Tau-A152T mutation. Finally, our observations of neuronal toxicity are broadly consistent with the neurotoxicity reported for human-induced pluripotent stem cells (iPSCs) carrying the Tau-A152T mutation [61].

As the phenotype suggests, enhanced extracellular glutamate concentrations in the hTau^{AT} slice medium may be caused by an increase in presynaptic release (as revealed by the effect of tetanus toxin, which reduces the increase in extracellular glutamate in hTau^{AT} slices to control levels). However, electrophysiology demonstrated that paired-pulse ratios are unaffected arguing against presynaptic vesicle release enhancement due to hTau^{AT} expression, but leaving the possibility that extracellular glutamate increase is due to an increase in total number of presynaptic release sites. Additionally, a dysfunction of the glutamate transporter EAAT2/GLT1 in astrocytes may contribute to the observed increase in extracellular glutamate levels as revealed by pharmacological application of the EAAT2/GLT1 blocker TBOA. Dysregulation of glutamate was also reported in other tau transgenic mouse lines [25,62]. Glutamate is largely taken up by astrocytic glutamate transporters (EAAT2/GLT1), but in many neurodegenerative diseases the expression of the EAAT2/GLT1 is reduced [63,64] and mice expressing mutant tau P301L show lower EAAT2/GLT1 expression levels [25]. Indeed, in our slice system the activation of EAAT2/GLT1 by ceftriaxone [47] was able to preserve normal intracellular calcium levels and extracellular glutamate levels; it prevented neurotoxicity and mitigated epileptiform activity to control levels. However, transcription levels of EAAT2/GLT1 remained unchanged in hTau^{AT}-expressing mice (Fig EV4E).

In conclusion, the pathological effects of the hTau^{AT} mutation are explained by an enhanced presynaptic glutamate release which results in an overactivation of NR2B-containing, extrasynaptic NMDA receptors that finally initiate an excitotoxic cascade ending up with CREB shutoff and neuronal death. The pathology can be ameliorated by lowering extracellular glutamate (e.g., by enhancing glutamate re-uptake into astrocytes by ceftriaxon), or by de-sensitizing extrasynaptic NR2B receptors (e.g., memantine).

Materials and Methods

Generation of hTau^AT mice

To achieve ubiquitous transgene expression in the brain at moderate levels, the transgene (human full-length Tau carrying the mutation A152T) was inserted into the ROSA locus of C57BL/6NTac embryo stem (ES) cells and injected C57BL/6NTac ES cells into BALB/c blastocysts (TACONIC, Germantown, NY). Injected blastocysts were transferred into the uterine horn of pseudopregnant NMR1 females. Chimerism was determined in chimeras by coat color contribution of ES cells to the BALB/c host (black/white). Highly chimeric mice were bred to C57BL/6 females. Germline transmission was identified by the presence of black offspring. The transgene expression is controlled by the neuron-specific Thy1.2 promoter and occurs in the entire brain and spinal cord. The mouse strain was conceived on an identical C57BL/6N background. The present study presents data from heterozygous and homozygous hTau^AT mice. Non-transgenic littermates were used as negative controls. All animals were housed and tested according to the standards of the German Animal Welfare Act.

Genotyping of hTau^AT mice

The hTau^AT mice (hetero- or homozygous) were identified by PCR of genomic mouse tail DNA using the primer pair 5′-AGCACCCTTAGTGGATGAGG-3′ and 5′-TTGTCATCGCTTCCAGTCC-3′, which amplified an expected DNA fragment of 192 bp (human Tau construct). Heterozygous and non-transgenic littermates differ by the appearance of the 299 bp control fragment (ROSA26-locus) amplified by the primer pair 5′-CTCTTCCCTCGTGATCTGCAACTCC-3′ and 5′-CATGTCTTTAATCTACCTCGATGG-3′ to homozygous hTau^AT.

Biochemical analysis of mice

Mice were anesthetized with a O_2/CO_2 mixture and killed by decapitation. Sarcosyl extraction, total protein preparation, and Western blots were performed as described previously [29]. About 3 μg of total protein or 3 μl of sarcosyl extraction lysates from different tissues (cortex and hippocampus) were loaded for the detection with the pan-Tau antibody K9JA (1:20,000, Dako). Blots were normalized by the concentration of β-actin (1:20,000, Sigma), visualized with ECL Plus detection system (GE Healthcare), and analyzed by densitometry (LAS 3000, AIDA software). For the analysis of NeuN (antibody 1:1,000, Millipore) expression, 5 μg of total protein from hippocampal tissue was loaded. Blots were normalized by the concentration of GAPDH (antibody 1:60,000, Sigma).

Real-time PCR

The RNA extraction was performed by using a standard Trizol/1-bromo-3-chloropropane extraction protocol followed by cDNA generation using the first strand cDNA synthesis kit (Thermo Scientific). RNA was extracted from hippocampus homogenates of 16-month-old heterozygous and homozygous animals and control littermates (for all groups $n = 4$ animals were analyzed). The Primer3Plus program was used for primer design [65]. Primers were required to be intron spanning and to be yielding an amplicon of 70–120 basepair. The three most stable housekeeping genes were selected (out of a group of five commonly used housekeeping genes) based on the geNorm value [66]. The qPCR analysis was done using the IQ5 optical system real-time PCR machine (BIO-RAD) and the Maxima SYBR Green qPCR Master Mix (Thermo). The raw fluorescence data were exported to Excel (Microsoft) after which mRNA levels were determined based on an assumption free analysis by processing the raw fluorescence data with the LinRegPCR program [67]. A list of primers is found in Table 1.

Immunohistological analysis of mice

Immunohistochemistry was performed on 5-μm paraffin sections as described previously [29]. Brains were placed into histofix (Roth; 4% formalin for 24 h) and dehydrated by sequential incubation in a series of ethanols and chloroform. Sagittal brain sections were incubated with primary antibody prepared in 1% horse serum overnight at 4°C. The following antibodies were used: human Tau-specific antibody HT7 (1:2,000, Thermo Fisher Scientific, Waltham, MA, USA), AT180 (pThr231/pSer235, 1:500, Pierce, Rockford, USA), AT8 (pSer202/pThr205, 1:500, Thermo Scientific), NeuN (1:1,000, Millipore), Alz-50 (1:50), and PHF-1 (1:50, both gifts from Dr. P. Davies, Albert Einstein College, NY, USA). Rabbit polyclonal peptide antibody was generated against pT217 (1:1,000, Biosource, Camarillo, CA, USA). Counterstaining with hematoxylin (Roth, Karlsruhe, Germany) was performed according to the company instructions.

Gallyas silver staining

A total of 5-μm-thick paraffin sections were stained as published [68].

Table 1. Primers.

Gene	Full name	Alias	Sequence (forward)	Sequence(reverse)	TM
hTau40 A152T	human tau full-length with A152T substitution	hTau^AT	ATCGACATGGTAGACTCGCC	TGACCGGGAGAAGCAAGAC	
Fos	FBJ osteosarcoma oncogene	cFOS	TCCTACTACCATTCCCCAGC	ATAAAGTTGGCACTAGAGACGG	60°
Homer1a	homer homolog 1 (*Drosophila*)	Vesl-1S	GTTTGAACTGCATTAATAGGGC	GTCATCCCTAACTTCCTTGTTCC	60°
Rbfox3	RNA binding protein, fox-1 homolog (*C. elegans*) 3	NeuN	GTAGAGGGACGGAAAATTGAG	ATAGACTGTTCCTACCACAGGG	60°
Grin2a	Glutamate receptor, ionotropic, NMDA2A (epsilon 1)	NR2A	ATGGGAAGCATGGGAAAAAGG	CACGGCCATAACTGCTCG	60°
Grin2b	Glutamate receptor, ionotropic, NMDA2B (epsilon 2)	NR2B	TTCCGACATTGCTTCATGGG	TAGCTACTCCGTGGATACAGC	60°
Slc1a2	Solute carrier family 1 (glial high affinity glutamate transporter), member 2	EAAT2	GGAGAACCTGGTGCAAGC	TTCAACATGGAGATGACCGC	60°

Transmission electron microscopy

Heterozygous hTau[AT] mice (hTau[AT] mice as described above were crossed with black C57Bl/6N background to Gfap-luc mice with a white FVB/N background receiving mice with a brown coat color and mixed background 50:50) and controls only carrying the reporter gene but not the mutation (12–13 months old) in groups ($n = 4$) were terminally anesthetized using ketamine–xylazine and euthanized by perfusion fixation for transmission electron microscopy as described previously [69]. Sections were examined using a Zeiss LEO922 transmission electron microscope with a 2k-CCD camera and subsequently processed using Adobe Photoshop software (Adobe Systems Incorporated, San Jose, CA, USA).

Golgi staining and dendritic spine counting

For Golgi-Cox impregnation of neurons [70], the FD rapid GolgiStain TM kit (FD NeuroTechnologies, Columbia, MD, USA) was used according to the manufacturer's protocol. A total of 80-μm floating sections of transgenic and WT mice at 10 months of age were Golgi-impregnated and hippocampal pyramidal CA3-neurons were used for quantification of dendritic spines as described [71]. The number of animals used for spine quantification was four for heterozygous A152T mice, while two littermate control animals were used for spine counting. An average of 5 dendrites of CA3 pyramidal neurons were analyzed per animal. The sections were imaged using the FV-1000 microscope (Olympus, Shinjuku, Tokyo, Japan) in stacks by application of a 60× objective and a 5× digital zoom. Stacks were loaded in NeuronStudio (CNIC, NY, USA) and inverted after which the dendrite length and spine detection was done in an automated fashion with the trainable spine classifier. Groups were compared and tested for statistically significant difference by applying an unpaired *t*-test.

Hippocampal organotypic slice cultures

Hippocampal organotypic slice cultures were prepared as described [72], with modifications [16]. Briefly, 8-day-old mice were decapitated, brains were rapidly removed, and hippocampi dissected at 4°C. A McIIwain tissue chopper (Gabler, Bad Schwabach, Germany) was used to prepare 400-μm-thick transverse slices which were transferred to semiporous cell culture inserts (Millipore, Bedford, MA, USA; 0.4 mm). Inserts containing 6–8 slices were placed in 6-well culture trays containing 1 ml of culture media (50% Minimum Essential Medium (MEM), 25% Hank's Balanced Salt Solution (HBSS), penicillin/streptomycin (all from PAA, Pasching, Austria), 25% horse serum, 4.5 mg/ml glucose (Sigma-Aldrich, St. Louis, MO, USA), pH 7.4). The culture medium was changed on the first day after preparation and afterward every third day. Slices were kept in culture for up to 60 days.

Ca²⁺ imaging

Ca²⁺ imaging experiments of organotypic slices (at 15 DIV) were performed as described previously [16]. Briefly, slices were loaded with Fura-2AM (Invitrogen, Carlsbad, CA, USA) at a concentration of 100 μM at 37°C for 30 min. After loading, slices were washed with 4-(2-hydroxyethyl)-1-piperazineethane sulfonic acid (HEPES)-buffered saline (130 mM NaCl, 5.4 mM KCl; 10 mM HEPES, 25 mM glucose, 1.8 mM $CaCl_2$, 1 mM $MgCl_2$; pH 7.4) for another 30 min to allow complete de-esterification of the Fura dye. After washing, cultures were transferred to a submerged imaging chamber of an Examiner A1 microscope (Zeiss, Jena, Germany). Fura-2 fluorescence was imaged at room temperature (RT) in HEPES-buffered saline, using a 10× water immersion objective. The emission of Fura-2-loaded pyramidal neurons was collected at 510 nm after excitation at 340 and 380 nm, respectively, with a Sutter DCIV shutter (Sutter Instrument Co, Navato, CA, USA). Images were taken at a rate of 1 Hz. For baseline recording, intracellular Ca^{2+} levels were imaged for a 30-s period following superfusion with high potassium (HEPES-buffered saline containing 180 mM KCl) for an additional 30 s. Analysis was performed offline, using 10 regions of interest with constant diameter in area CA3. For each slice, we performed an internal background subtraction, averaged the values in the regions of interest, and normalized with their individual baseline value. Absolute intracellular Ca^{2+} concentrations were calculated from the ratio of emitted fluorescence (510 nm) after excitation at 340 nm and 380 nm with the standard Grynkiewicz formula [73]. The Kd value was calculated by using Invitrogen Fura-2 calibration kit. Initially, Ca^{2+} imaging was performed in a blinded fashion to compare control littermate slices with slices expressing hTau[AT] without drug application.

Microscopy

Images were acquired with an Olympus laser scanning microscope FV1000 (Olympus, Tokyo, Japan), equipped with a confocal laser scanning unit, argon (Ar; 488 nm) and helium/neon (He/Ne 543 nm and 633 nm). For 2 or 3 channel imaging, images were acquired via sequential scanning. Maximum projection images were generated from resulting *z*-stacks using ImageJ software (NIH, Bethesda, MD, USA).

DiI labeling of slice cultures and spine counting

Hippocampal slice cultures were fixed at DIV 20 in 4% PFA for 2 h, still attached to the semiporous cell culture inserts. A DiI crystal was placed on the CA3 region followed by an incubation of 10 days at room temperature in 4% PFA to allow diffusion. Dendritic spines were imaged by confocal microscopy using tetramethyl rhodamine isothiocyanate (TRITC)-filter settings. ImageJ (NIH, USA) was used to measure spine density from resulting *z*-stacks.

Cytotoxicity and glutamate assay

Cytotoxicity was assessed by the lactate dehydrogenase (LDH) assay (Cytotoxicity Detection Kit (Roche Diagnostics, Mannheim, Germany)). Slice cultures were incubated in serum-free culture medium. The medium was collected at different time points *in vitro* and processed as prescribed. Finally, the absorbance at 492 nm (indicating dying cells) was assayed in 96-well plates (plate reader Tecan Safire, Männedorf, Switzerland). The amount of glutamate in the culture medium (serum and glutamate free) was determined with the Amplex Red Glutamic Acid/Glutamate Oxidase Assay Kit

(Molecular Probes, US). Medium was collected at different time points *in vitro* and treated as prescribed. Caspase-3 activity was determined fluorometrically by the EnzChek Caspase-3 Assay Kit with Z-DEVD-AMC substrate (Molecular Probes). Pooled slice cultures (6 slices per sample) were homogenized and treated as prescribed. The assay was performed in 96-well microplates and read on a fluorescence plate reader (Tecan Safire) at excitation 342 nm and emission 441 nm.

Immunohistological analysis of slice cultures

Slice cultures were attached on the Millicell membrane and stained as free-floating sections in 6-well plates. Cultures were first fixed with 4% paraformaldehyde (PFA) in phosphate-buffered saline (PBS) (PAA, Austria) for 2 h at 4°C. After washing with PBS, slices were permeabilized by 0.1% Triton X-100/PBS for 90 min at RT. Slices were then blocked with 5% bovine serum albumin (BSA) for 2 h and afterward incubated with primary antibody diluted in PBS for 3 days at 4°C. After washing three times with PBS, slices were incubated with secondary antibody for 3 days at 4°C. Finally, slices were incubated with the nuclear counterstain and dead cell indicator TO-PRO3 (Thermo Fisher Scientific, Waltham, MA, USA) for 15 min and washed three times with PBS before getting mounted with Permafluor mounting solution (Beckman Coulter, Paris, France) and cover-slipped. The following primary antibodies were used: monoclonal anti-neuronal nuclei (NeuN) antibody (Chemicon International, Temecula, CA, USA) (1:500), pan-Tau antibody K9JA (Dako, Hamburg, Germany, Nr. A0024 (1:1,000)), microtubule associated protein 2a/b (MAP2a/b) antibody (AP20; Sigma-Aldrich, Germany, 1:200), human-specific TauY9 (Enzo Life Sciences, Germany, 1:500); and PHF1 antibody for phosphorylated S396/404 Tau (gift from Dr. Peter Davies, Albert Einstein College, NY, US, 1:50); all fluorescent (goat anti-rabbit/mouse cyanine 2, 3 and 5)-labeled secondary antibodies were from Dianova (Hamburg, Germany) (1:1,000).

Drug application

For Ca^{2+} imaging, slices were incubated with the following drugs 120 min before and during Fura-2AM experiments: 20 μM L-VGCC inhibitor Nifedipine (Tocris Biosciences, Bristol, UK); 100 μM NMDAR blocker APV (Tocris Biosciences, Bristol, UK); 30 μM AMPAR antagonist CNQX (Tocris Biosciences, US); 20 μM NR2B-containing NMDA receptor antagonist Ifenprodil (Tocris Biosciences, Bristol, UK); 1 μM sodium channel blocker Tetrodotoxin (TTX) or 8 μM NMDA receptor antagonist memantine. For glutamate and LDH release assays, drugs were administered from DIV 1 until DIV 25 or DIV 30. During treatment, the drug was refreshed every 3rd day, simultaneously with full medium change. The following drugs were used: 1 μM TTX, 100 μM EAAT2/GLT1 activator ceftriaxone; 50 nM tetanus neurotoxin (TeNT) or memantine (8 μM). TBOA (50 μM; Tocris Biosciences, Bristol, UK) and DCGIV (5 μM; Tocris Biosciences, Bristol, UK).

Biochemical analysis of slice cultures

To estimate protein expression, cultured hippocampal slices (6–8, prepared and pooled from the same animal) were homogenized in lysis buffer [50 mM Tris–HCl, pH 7.4, 10% glycerol, 1% NP-40, 5 mM DTT, 1 mM EGTA, 20 mM NaF, 1 mM Na_3VO_4, 150 mM NaCl, protease inhibitors (Complete Mini; Roche, Indianapolis, IN), 100 U/ml benzonase, 5 μM okadaic acid, 5 mM CHAPS (3-[(3-cholamidopropyl)dimethylammonio]-1-propanesulfonate)]. Total protein extracts were resolved by SDS–PAGE (10% polyacrylamide gels) and transferred to polyvinylidene fluoride (PVDF) membranes (Millipore, Bedford, MA, USA). The membrane was incubated in 5% non-fat milk in TBS-Tween for 1 h at RT, washed with TBS-Tween and incubated overnight in primary antibody solution at 4°C. The membrane was washed with TBS-Tween and incubated with the secondary antibody (Dako, Hamburg, Germany) coupled to horseradish peroxidase (HRP) for 1 h at RT. The membrane was developed by ECL Western Blotting Detection Kit (GE Healthcare, Chalfont St Giles, UK) and analyzed by densitometry (LAS 3000; AIDA software; Raytest, Straubenhardt, Germany). The following antibodies were used: pan-Tau antibody K9JA (DAKO, Hamburg, A-0024) (1:10,000), anti-β-actin (Sigma, Germany) (1:10,000)), anti-CREB (Cell Signaling) (1:1,000), and anti-p133 CREB (Cell Signaling, Darmstadt, Germany) (1:1,000) and secondary antibodies, HRP-anti-rabbit and HRP-anti-mouse (DakoCytomation, Carpinteria, CA, USA) (1:1,000).

Electrophysiology

Acute, transverse hippocampal slices were prepared from 12(±1)-month-old male and female mice anaesthetized for approximately 15 s by isoflurane inhalation before decapitation. To obtain optimal mossy fiber preservation, a cutting angle of 12° in the fronto-occipital direction was used [74] for vibrating-blade microtome (VS1200T; Leica, Wetzlar, Germany) sectioning. A total of 350-μm-thick slices were transferred into a custom-made interface chamber and superfused with carbogenated ACSF (126 mM NaCl, 26 mM $NaHCO_3$, 3 mM KCl, 2.5 mM $CaCl_2$, 1.3 mM $MgSO_4$, 1.25 mM NaH_2PO_4 and 10 mM glucose, saturated with 95% O_2/5% CO_2) at 36 ± 0.5°C; flow rate, 1.8–3 ml/min; pH 7.4. After 1.5-h recovery, slices were transferred to a submerged recording chamber at 30°C. Extracellular field potentials (fEPSP) were recorded from stratum lucidum in area CA3 at a flow rate of ~5 ml/min. The mossy fiber tract was visualized by infrared (IR)/differential interference contrast (DIC) microscopy. As stimulation electrode, a patch-clamp pipette was used (1–2 MΩ) to excite mossy fibers (mf) in the region of the hilus. Recording electrodes (2.5–3 MΩ) were filled with ACSF and separated constantly 200 μm from each other. fEPSPs were 10× preamplified (custom-made preamplifier) filtered at 1 kHz and sampled at 10 kHz using a HEKA double patch-clamp EPC 10 USB amplifier (HEKA Elektronik Dr. Schulze GmbH, Lambrecht, Germany). Organotypic hippocampal slices were recorded at DIV 10 and 30 with the same ACSF composition, temperature, and electrodes as described above.

Stimulation and recording procedures

Constant current pulses were elicited every 20 s (0.05 Hz) with a pulse width of 0.1 ms. Input/output (I/O) curves were generated using stimulus intensities ranging from 10 to 100 μA with an increment of 10 μA. In the same slice, paired-pulse facilitation (PPF) was

evoked by a 50-ms interstimulus interval (ISI). In a next step, frequency facilitation (FF) of the mossy fiber pathway was measured by switching stimulation frequency from 0.1 to 1 Hz. Only slices which showed robust FF were used further on for mf-LTP recordings. LTP was induced by theta burst stimulation at 30% of the maximum stimulus intensity as revealed initially during the I/O recording. At the end of each recording, 5 μM DCGIV (Tocris Biosciences, Bristol, UK) was applied for at least 5 min to test mossy fiber specificity. In case the fEPSP slope was not reduced to more than 50% of the initial slope steepness, slices were excluded from further mossy fiber analysis.

Statistical analysis

Statistical analysis was performed by using the statistics software Prism5 (GraphPad, La Jolla, CA, USA). Evaluation of data was performed either by Student's *t*-test or one-way ANOVA followed by Tukey's *post hoc* test or Newman–Keuls multiple comparison test or multiple repeat ANOVA (Statistica, Statsoft (Europe), Hamburg, Germany) as indicated. If not indicated, *P*-values display Student's *t*-test. Data are shown as mean ± SEM. *P*-values are as follows: *$P < 0.05$, **< 0.01, and ***$P < 0.001$.

Expanded View for this article is available online.

Author contributions

JMD performed electrophysiological experiments in acute and organotypic slices, calcium imaging in slice cultures as well as analysis, experiment design, writing of the manuscript, and figure artwork. LK contributed immunfluorescence, biochemistry, and calcium imaging in organotypic slices as well as analysis, experiment design, writing of the manuscript, and figure artwork. AS performed biochemical and immunohistochemical analysis of adult transgenic mice. FJAD performed quantitative real-time PCR and dendritic spine analysis in adult mice. ZS carried out EM experiments and analysis. EM and E-MM supervised the study and writing of the manuscript.

Conflict of interest

The authors declare that they have no conflict of interest.

References

1. Goedert M, Crowther RA, Spillantini MG (1998) Tau mutations cause frontotemporal dementias. *Neuron* 21: 955−958
2. Barghorn S, Zheng-Fischhofer Q, Ackmann M, Biernat J, von Bergen M, Mandelkow EM, Mandelkow E (2000) Structure, microtubule interactions, and paired helical filament aggregation by tau mutants of frontotemporal dementias. *Biochemistry* 39: 11714−11721
3. Hong M, Zhukareva V, Vogelsberg-Ragaglia V, Wszolek Z, Reed L, Miller BI, Geschwind DH, Bird TD, McKeel D, Goate A *et al* (1998) Mutation-specific functional impairments in distinct tau isoforms of hereditary FTDP-17. *Science* 282: 1914−1917
4. Kovacs GG, Molnar K, Laszlo L, Strobel T, Botond G, Honigschnabl S, Reiner-Concin A, Palkovits M, Fischer P, Budka H (2011) A peculiar constellation of tau pathology defines a subset of dementia in the elderly. *Acta Neuropathol* 122: 205−222
5. Kara E, Ling H, Pittman AM, Shaw K, deSilva R, Simone R, Holton JL, Warren JD, Rohrer JD, Xiromerisiou G *et al* (2012) The MAPT p.A152T variant is a risk factor associated with tauopathies with atypical clinical and neuropathological features. *Neurobiol Aging* 33: 2231 e7−2231 e14
6. Lee SE, Tartaglia MC, Yener G, Genc S, Seeley WW, Sanchez-Juan P, Moreno F, Mendez MF, Klein E, Rademakers R *et al* (2013) Neurodegenerative disease phenotypes in carriers of MAPT p. A152T, a risk factor for frontotemporal dementia spectrum disorders and Alzheimer disease. *Alzheimer Dis Assoc Disord* 27: 302−309
7. Coppola G, Chinnathambi S, Lee JJ, Dombroski BA, Baker MC, Soto-Ortolaza AI, Lee SE, Klein E, Huang AY, Sears R *et al* (2012) Evidence for a role of the rare p. A152T variant in MAPT in increasing the risk for FTD-spectrum and Alzheimer's diseases. *Hum Mol Genet* 21: 3500−3512
8. Binder LI, Frankfurter A, Rebhun LI (1985) The distribution of tau in the mammalian central nervous system. *J Cell Biol* 101: 1371−1378
9. Brion JP, Guilleminot J, Couchie D, Flament-Durand J, Nunez J (1988) Both adult and juvenile tau microtubule-associated proteins are axon specific in the developing and adult rat cerebellum. *Neuroscience* 25: 139−146
10. Gotz J, Ittner LM, Kins S (2006) Do axonal defects in tau and amyloid precursor protein transgenic animals model axonopathy in Alzheimer's disease? *J Neurochem* 98: 993−1006
11. Thies E, Mandelkow EM (2007) Missorting of tau in neurons causes degeneration of synapses that can be rescued by the kinase MARK2/Par-1. *J Neurosci* 27: 2896−2907
12. Hoover BR, Reed MN, Su J, Penrod RD, Kotilinek LA, Grant MK, Pitstick R, Carlson GA, Lanier LM, Yuan LL *et al* (2010) Tau mislocalization to dendritic spines mediates synaptic dysfunction independently of neurodegeneration. *Neuron* 68: 1067−1081
13. Ittner LM, Ke YD, Delerue F, Bi M, Gladbach A, van Eersel J, Wolfing H, Chieng BC, Christie MJ, Napier IA *et al* (2010) Dendritic function of tau mediates amyloid-beta toxicity in Alzheimer's disease mouse models. *Cell* 142: 387−397
14. Polydoro M, Dzhala VI, Pooler AM, Nicholls SB, McKinney AP, Sanchez L, Pitstick R, Carlson GA, Staley KJ, Spires-Jones TL *et al* (2014) Soluble pathological tau in the entorhinal cortex leads to presynaptic deficits in an early Alzheimer's disease model. *Acta Neuropathol* 127: 257−270
15. Decker JM, Kruger L, Sydow A, Zhao S, Frotscher M, Mandelkow E, Mandelkow EM (2015) Pro-aggregant Tau impairs mossy fiber plasticity due to structural changes and Ca^{2+} dysregulation. *Acta Neuropathol Commun* 3: 23
16. Messing L, Decker JM, Joseph M, Mandelkow E, Mandelkow EM (2013) Cascade of tau toxicity in inducible hippocampal brain slices and prevention by aggregation inhibitors. *Neurobiol Aging* 34: 1343−1354
17. Zempel H, Thies E, Mandelkow E, Mandelkow EM (2010) Abeta oligomers cause localized Ca(2+) elevation, missorting of endogenous Tau into dendrites, Tau phosphorylation, and destruction of microtubules and spines. *J Neurosci* 30: 11938−11950

18. Morris M, Maeda S, Vossel K, Mucke L (2011) The many faces of tau. *Neuron* 70: 410–426

19. Vossel KA, Xu JC, Fomenko V, Miyamoto T, Suberbielle E, Knox JA, Ho K, Kim DH, Yu GQ, Mucke L (2015) Tau reduction prevents Abeta-induced axonal transport deficits by blocking activation of GSK3beta. *J Cell Biol* 209: 419–433

20. Roberson ED, Halabisky B, Yoo JW, Yao J, Chin J, Yan F, Wu T, Hamto P, Devidze N, Yu GQ *et al* (2011) Amyloid-beta/Fyn-induced synaptic, network, and cognitive impairments depend on tau levels in multiple mouse models of Alzheimer's disease. *J Neurosci* 31: 700–711

21. Holth JK, Bomben VC, Reed JG, Inoue T, Younkin L, Younkin SG, Pautler RG, Botas J, Noebels JL (2013) Tau loss attenuates neuronal network hyperexcitability in mouse and *Drosophila* genetic models of epilepsy. *J Neurosci* 33: 1651–1659

22. Hauw JJ, Daniel SE, Dickson D, Horoupian DS, Jellinger K, Lantos PL, McKee A, Tabaton M, Litvan I (1994) Preliminary NINDS neuropathologic criteria for Steele-Richardson-Olszewski syndrome (progressive supranuclear palsy). *Neurology* 44: 2015–2019

23. Amadoro G, Ciotti MT, Costanzi M, Cestari V, Calissano P, Canu N (2006) NMDA receptor mediates tau-induced neurotoxicity by calpain and ERK/MAPK activation. *Proc Natl Acad Sci USA* 103: 2892–2897

24. Nilsen LH, Rae C, Ittner LM, Gotz J, Sonnewald U (2013) Glutamate metabolism is impaired in transgenic mice with tau hyperphosphorylation. *J Cereb Blood Flow Metab* 33: 684–691

25. Hunsberger HC, Rudy CC, Batten SR, Gerhardt GA, Reed MN (2015) P301L tau expression affects glutamate release and clearance in the hippocampal trisynaptic pathway. *J Neurochem* 132: 169–182

26. Nygaard TG, Duvoisin RC, Manocha M, Chokroverty S (1989) Seizures in progressive supranuclear palsy. *Neurology* 39: 138–140

27. Maeda S, Djukic B, Taneja P, Yu G, Lo I, Davis A, Craft R, Guo W, Wang X, Kim D *et al* (2016) Expression of A152T human tau causes age-dependent neuronal dysfunction and loss in transgenic mice. *EMBO Rep* 17: 530–551

28. Bouabe H, Okkenhaug K (2013) A protocol for construction of gene targeting vectors and generation of homologous recombinant embryonic stem cells. *Methods Mol Biol* 1064: 337–354

29. Mocanu MM, Nissen A, Eckermann K, Khlistunova I, Biernat J, Drexler D, Petrova O, Schonig K, Bujard H, Mandelkow E *et al* (2008) The potential for beta-structure in the repeat domain of tau protein determines aggregation, synaptic decay, neuronal loss, and coassembly with endogenous Tau in inducible mouse models of tauopathy. *J Neurosci* 28: 737–748

30. Siskova Z, Justus D, Kaneko H, Friedrichs D, Henneberg N, Beutel T, Pitsch J, Schoch S, Becker A, von der Kammer H *et al* (2014) Dendritic structural degeneration is functionally linked to cellular hyperexcitability in a mouse model of Alzheimer's disease. *Neuron* 84: 1023–1033

31. Foster KA, McLaughlin N, Edbauer D, Phillips M, Bolton A, Constantine-Paton M, Sheng M (2010) Distinct roles of NR2A and NR2B cytoplasmic tails in long-term potentiation. *J Neurosci* 30: 2676–2685

32. Barria A, Malinow R (2002) Subunit-specific NMDA receptor trafficking to synapses. *Neuron* 35: 345–353

33. Barria A, Malinow R (2005) NMDA receptor subunit composition controls synaptic plasticity by regulating binding to CaMKII. *Neuron* 48: 289–301

34. Korinek M, Kapras V, Vyklicky V, Adamusova E, Borovska J, Vales K, Stuchlik A, Horak M, Chodounska H, Vyklicky L Jr (2011) Neurosteroid modulation of N-methyl-D-aspartate receptors: molecular mechanism and behavioral effects. *Steroids* 76: 1409–1418

35. Xia P, Chen HS, Zhang D, Lipton SA (2010) Memantine preferentially blocks extrasynaptic over synaptic NMDA receptor currents in hippocampal autapses. *J Neurosci* 30: 11246–11250

36. Cull-Candy SG, Leszkiewicz DN (2004) Role of distinct NMDA receptor subtypes at central synapses. *Sci STKE* 2004: re16

37. Cull-Candy S, Brickley S, Farrant M (2001) NMDA receptor subunits: diversity, development and disease. *Curr Opin Neurobiol* 11: 327–335

38. Hardingham GE, Bading H (2010) Synaptic versus extrasynaptic NMDA receptor signalling: implications for neurodegenerative disorders. *Nat Rev Neurosci* 11: 682–696

39. Paoletti P, Bellone C, Zhou Q (2013) NMDA receptor subunit diversity: impact on receptor properties, synaptic plasticity and disease. *Nat Rev Neurosci* 14: 383–400

40. Parsons MP, Raymond LA (2014) Extrasynaptic NMDA receptor involvement in central nervous system disorders. *Neuron* 82: 279–293

41. Talantova M, Sanz-Blasco S, Zhang X, Xia P, Akhtar MW, Okamoto S, Dziewczapolski G, Nakamura T, Cao G, Pratt AE *et al* (2013) Abeta induces astrocytic glutamate release, extrasynaptic NMDA receptor activation, and synaptic loss. *Proc Natl Acad Sci USA* 110: E2518–E2527

42. Hara MR, Snyder SH (2007) Cell signaling and neuronal death. *Annu Rev Pharmacol Toxicol* 47: 117–141

43. Mantamadiotis T, Lemberger T, Bleckmann SC, Kern H, Kretz O, Martin Villalba A, Tronche F, Kellendonk C, Gau D, Kapfhammer J *et al* (2002) Disruption of CREB function in brain leads to neurodegeneration. *Nat Genet* 31: 47–54

44. Barco A, Bailey CH, Kandel ER (2006) Common molecular mechanisms in explicit and implicit memory. *J Neurochem* 97: 1520–1533

45. Yuste R, Bonhoeffer T (2001) Morphological changes in dendritic spines associated with long-term synaptic plasticity. *Annu Rev Neurosci* 24: 1071–1089

46. Nabavi S, Fox R, Proulx CD, Lin JY, Tsien RY, Malinow R (2014) Engineering a memory with LTD and LTP. *Nature* 511: 348–352

47. Rothstein JD, Patel S, Regan MR, Haenggeli C, Huang YH, Bergles DE, Jin L, Dykes Hoberg M, Vidensky S, Chung DS *et al* (2005) Beta-lactam antibiotics offer neuroprotection by increasing glutamate transporter expression. *Nature* 433: 73–77

48. Morgan JI, Cohen DR, Hempstead JL, Curran T (1987) Mapping patterns of c-fos expression in the central nervous system after seizure. *Science* 237: 192–197

49. Ronesi JA, Collins KA, Hays SA, Tsai NP, Guo W, Birnbaum SG, Hu JH, Worley PF, Gibson JR, Huber KM (2012) Disrupted Homer scaffolds mediate abnormal mGluR5 function in a mouse model of fragile X syndrome. *Nat Neurosci* 15: 431–440, S1

50. Tang AH, Alger BE (2015) Homer protein-metabotropic glutamate receptor binding regulates endocannabinoid signaling and affects hyperexcitability in a mouse model of fragile X syndrome. *J Neurosci* 35: 3938–3945

51. Danbolt NC (2001) Glutamate uptake. *Prog Neurobiol* 65: 1–105

52. Moddel G, Jacobson B, Ying Z, Janigro D, Bingaman W, Gonzalez-Martinez J, Kellinghaus C, Prayson RA, Najm IM (2005) The NMDA receptor NR2B subunit contributes to epileptogenesis in human cortical dysplasia. *Brain Res* 1046: 10–23

53. Li Z, Hall AM, Kelinske M, Roberson ED (2014) Seizure resistance without parkinsonism in aged mice after tau reduction. *Neurobiol Aging* 35: 2617–2624

54. Xu CS, Liu AC, Chen J, Pan ZY, Wan Q, Li ZQ, Wang ZF (2015) Over-activation of NR2B-containing NMDA receptors through entorhinal-hippocampal connection initiates accumulation of hyperphosphorylated

tau in rat hippocampus after transient middle cerebral artery occlusion (MCAO). *J Neurochem* 134: 566–577

55. Van der Jeugd A, Hochgrafe K, Ahmed T, Decker JM, Sydow A, Hofmann A, Wu D, Messing L, Balschun D, D'Hooge R *et al* (2012) Cognitive defects are reversible in inducible mice expressing pro-aggregant full-length human Tau. *Acta Neuropathol* 123: 787–805

56. Sydow A, Van der Jeugd A, Zheng F, Ahmed T, Balschun D, Petrova O, Drexler D, Zhou L, Rune G, Mandelkow E *et al* (2011) Tau-induced defects in synaptic plasticity, learning, and memory are reversible in transgenic mice after switching off the toxic Tau mutant. *J Neurosci* 31: 2511–2525

57. Furukawa K, Wang Y, Yao PJ, Fu W, Mattson MP, Itoyama Y, Onodera H, D'Souza I, Poorkaj PH, Bird TD *et al* (2003) Alteration in calcium channel properties is responsible for the neurotoxic action of a familial fron-totemporal dementia tau mutation. *J Neurochem* 87: 427–436

58. Vossel KA, Beagle AJ, Rabinovici GD, Shu H, Lee SE, Naasan G, Hegde M, Cornes SB, Henry ML, Nelson AB *et al* (2013) Seizures and epileptiform activity in the early stages of Alzheimer disease. *JAMA Neurol* 70: 1158–1166

59. Ruan YW, Lei Z, Fan Y, Zou B, Xu ZC (2009) Diversity and fluctuation of spine morphology in CA1 pyramidal neurons after transient global ischemia. *J Neurosci Res* 87: 61–68

60. Bano D, Young KW, Guerin CJ, Lefeuvre R, Rothwell NJ, Naldini L, Rizzuto R, Carafoli E, Nicotera P (2005) Cleavage of the plasma membrane Na$^+$/Ca^{2+} exchanger in excitotoxicity. *Cell* 120: 275–285

61. Fong H, Wang C, Knoferle J, Walker D, Balestra ME, Tong LM, Leung L, Ring KL, Seeley WW, Karydas A *et al* (2013) Genetic correction of tauopathy phenotypes in neurons derived from human induced pluripo-tent stem cells. *Stem Cell Reports* 1: 226–234

62. Roberson ED, Scearce-Levie K, Palop JJ, Yan F, Cheng IH, Wu T, Gerstein H, Yu GQ, Mucke L (2007) Reducing endogenous tau ameliorates amyloid beta-induced deficits in an Alzheimer's disease mouse model. *Science* 316: 750–754

63. Masliah E, Alford M, Mallory M, Rockenstein E, Moechars D, Van Leuven F (2000) Abnormal glutamate transport function in mutant amyloid precursor protein transgenic mice. *Exp Neurol* 163: 381–387

64. Rothstein JD, Van Kammen M, Levey AI, Martin LJ, Kuncl RW (1995) Selective loss of glial glutamate transporter GLT-1 in amyotrophic lateral sclerosis. *Ann Neurol* 38: 73–84

65. Untergasser A, Nijveen H, Rao X, Bisseling T, Geurts R, Leunissen JA (2007) Primer3Plus, an enhanced web interface to Primer3. *Nucleic Acids Res* 35: W71–W74

66. Vandesompele J, De Preter K, Pattyn F, Poppe B, Van Roy N, De Paepe A, Speleman F (2002) Accurate normalization of real-time quantitative RT-PCR data by geometric averaging of multiple internal control genes. *Genome Biol* 3: RESEARCH0034

67. Ramakers C, Ruijter JM, Deprez RH, Moorman AF (2003) Assumption-free analysis of quantitative real-time polymerase chain reaction (PCR) data. *Neurosci Lett* 339: 62–66

68. Braak H, Braak E (1991) Neuropathological stageing of Alzheimer-related changes. *Acta Neuropathol* 82: 239–259

69. Siskova Z, Page A, O'Connor V, Perry VH (2009) Degenerating synaptic boutons in prion disease: microglia activation without synaptic strip-ping. *Am J Pathol* 175: 1610–1621

70. Glaser EM, Van der Loos H (1981) Analysis of thick brain sections by obverse-reverse computer microscopy: application of a new, high clarity Golgi-Nissl stain. *J Neurosci Methods* 4: 117–125

71. Ricobaraza A, Cuadrado-Tejedor M, Marco S, Perez-Otano I, Garcia-Osta A (2012) Phenylbutyrate rescues dendritic spine loss associated with memory deficits in a mouse model of Alzheimer disease. *Hippocampus* 22: 1040–1050

72. Stoppini L, Buchs PA, Muller D (1991) A simple method for organotypic cultures of nervous tissue. *J Neurosci Methods* 37: 173–182

73. Grynkiewicz G, Poenie M, Tsien RY (1985) A new generation of Ca^{2+} indicators with greatly improved fluorescence properties. *J Biol Chem* 260: 3440–3450

74. Behrens CJ, van den Boom LP, de Hoz L, Friedman A, Heinemann U (2005) Induction of sharp wave-ripple complexes in vitro and reorganization of hippocampal networks. *Nat Neurosci* 8: 1560–1567